Universiteit Antwerpen

Nitrogen fixation in an electrode-free microwave plasma

Nitrogen fixation in an electrode-free microwave plasma

Seán Kelly,[1,*,♣] and Annemie Bogaerts[1]

[1]Research group PLASMANT, Department of Chemistry, University of Antwerp, Belgium

*Correspondence: sean.kelly@uantwerpen.be

SUMMARY

Plasma-based gas conversion has great potential for enabling carbon-free fertiliser production powered by renewable electricity. Sustaining an energy-efficient plasma process without eroding the containment vessel is currently a significant challenge, limiting scaling to higher powers and throughputs. Isolation of the plasma from contact with any solid surfaces is an advantage, which both limits energy loss to the walls and prevents material erosion that could lead to disastrous soil contamination. This paper presents highly energy-efficient nitrogen fixation from air into NO_x by microwave plasma, with the plasma filament isolated at the centre of a quartz tube using a vortex gas flow. NO_x production is found to scale very efficiently when increasing both gas flow rate and absorbed power. The lowest energy cost recorded of ~2 MJ/mol, for a total NO_x production of ~3.8 %, is the lowest reported up to now for atmospheric pressure plasmas.

Keywords: plasma-based gas conversion, plasma produced fertiliser, air microwave plasma, plasma-based N_2 fixation, plasma NO_x production, Zeldovich mechanism.

INTRODUCTION

Higher global temperatures and increasing extreme weather events have brought the societal and economic perils of anthropogenic climate change to the fore in recent years. In this context, plasma technology is garnering increasing research interest[1,2]. Plasma-based gas conversion has great potential for enabling carbon-free fertiliser production in the agri-food sector[3]. These efforts are particularly timely and necessary, as economies face the challenge of transitioning to sustainable architectures based on eliminating anthropogenic greenhouse gases[4].

The increasing availability of renewables provides a 'clean' electricity source, ideally suited to plasma generation. Industrial scale nitrogen fixation (NF) via the Haber-Bosch (H-B) process dominates artificial fertiliser production, enabling crop yield enhancements, which at present nourish over 40% of the world population [5]. Owing to the exceptional stability of molecular nitrogen's triple bond, the H-B process is an energy-intensive chemical process, which accounts for 1-2 % of the world's energy consumption, consumes 2-3 % of the global natural gas output and emits more than 300 million tonnes of CO_2 annually[5]. In light of an increasing population (and fertiliser demand) coupled with an urgency to reduce CO_2 emissions, efforts to find alternative technologies for NF, that offer the potential of reduced energy usage while minimising greenhouse gas emissions, have accelerated. The fast ignition of plasma reactors (within the order of ~1 s) provides for a highly adaptable chemical process in the context of emerging renewable energy dominated electricity grids. This is in contrast to 'traditional' chemical processes, such as H-B, which require significant lead times (on the order of hours[6]), to schedule production and hence cannot benefit directly (i.e., without energy storage) from cost savings available by exploiting cheap 'peak-shaved' renewable electricity[5,7].

The Birkeland-Eyde (B-E) process to produce nitric acid was first developed in the early twentieth century[8-10]. The B-E process converted air to NO_x in an electric arc formed inside an electromagnet. Excess heat (i.e., not used in the enthalpy of formation) was partially reclaimed to heat boilers using the arc exhaust followed by an oxidation stage where the remaining NO is converted to NO_2 in settling tanks (i.e., this relatively slow reaction preferable at reduced temperatures). This stage is followed by NO_2 hydrolysis in large water absorption towers packed with quartz segments eventually producing a solution of HNO_3. The industrialised B-E process produced ~2 % NO_x and had an energy consumption for the NO_x plasma synthesis stage of 2.4–3.1 MJ/mol with the absorption stages adding approximately 30-40 % additional overhead[5,7,9].

While recent advances suggest that the energy cost and capital expenditure of the absorption stage could be significantly reduced, both in size and energy requirements (e.g., using modern NO_x absorbents such as BaO[11,12] in combination with temperature/ pressure swing absorption)[7], the critical energy hurdle of the plasma conversion stage still remains an open research challenge. The technological advances of the last century (such as the success of MW surface-wave plasmas in recent decades and the emergence of solid-state MW technology in recent years which are of particular relevance here) have motivated a revival of plasma-based NF in a contemporary context characterised by climate challenges and the emergence of renewable electricity.

♣ Lead contact

Microwave (MW) generated plasmas offer desirable characteristics[13] of high ionisation fraction (i.e., electron density) coupled with relatively low mean electron energies (in the range ~1-3 eV). The electric field generated by the applied MW power selectively heats the electrons, due to their small mass. Furthermore, the electron energy of 1-3 eV, combined with high electron density, gives rise to efficient vibrational excitation, which can in turn significantly promote dissociation routes in gases such as N_2[14]. Investigations in the early 1980s by *Asisov et al.*[15,16] employing a low pressure (10-100 Torr) Electron Cyclotron Resonance (ECR) MW discharge in N_2/O_2 mixes reported spectacular NO_x production levels of 14% at energy costs of 0.3 MJ/mol[15,16]. Many modern efforts have however focused on (near) atmospheric pressure discharges [7] (see state-of-the-art in **table 1**, in **section 3.1**). This is due to the high additional energy overhead associated with the use of vacuum pumps required to sustain low pressure conditions. Note that this cost was not accounted for in the above low pressure ECR plasma. Such extra energy costs typically eclipse any potential gains in conversion and efficiency available from operating at low pressures. For example, to reach ~100 Torr pressure (i.e., 13 % of atmospheric pressure) at a gas flow rate < 10 L/min would require at least the employment of a standard vacuum pump (e.g., rotary vane) which requires ~400 W power for operation[17]. This additional power requirement is similar to the typical power used to generate the plasma, indicating a doubling in energy cost when accounting for the use of a vacuum pump. Furthermore, the above spectacular NO_x production levels and energy costs reported for low pressure ECR MW plasmas[15,16] have never been reproduced since then.

Plasma-based NF can be carried out in pure N_2 gas streams (with subsequent reaction to produce NO_x or NH_3) or in N_2/O_2 or N_2/H_2 or N_2/H_2O mixes, where both gaseous and liquid H_2O can be employed[3,14,18-21]. In recent years, various studies have investigated the use of atmospheric pressure plasma for NF using air mixtures (N_2/O_2) (see state-of-the-art in **table 1** in **section 3.1**). *Kim et al.*[22] studied the use of a low powered MW plasma at pressures specified as 'slightly below atmospheric'. The authors used a titanium pin to aid ignition of the discharge at very modest powers from 60-90 W, achieving ~0.6 % NO_x at an energy cost of ~4 MJ/mol.

Non-MW plasma approaches of interest include gliding arc (GA) type discharges[14,23-28] where a heated and (typically) dynamic plasma arc is sustained using metallic electrodes with direct or alternating current (kHz) power sources[14,25]. Indeed, the GA approach has the best conversion and energy efficiency reported to-date for atmospheric pressure plasma-based NF (up to 5.5 % NOx production at < 3 MJ/mol energy cost[24]). Similar to MW plasmas, GA plasmas under atmospheric pressure are typically categorised as 'warm' plasmas (i.e., average gas temperatures ranging ~1000-3000 K), where significant gas heating offers the benefits of both non-thermal and thermal plasma conditions. The ability to scale this achievement to higher powers (i.e., > 500 W) and flow rates (i.e., >10 L/min), a key requirement to future industrial deployment, is however unclear.

Three-dimensional implementations of the GA concept, including the gliding arc plasmatron (GAP)[23,29] or the rotating gliding arc (RGA)[24,25,28,30], often employ a swirling flow. This typically results in a dynamic plasma filament which has benefited conversion metrics over earlier 2D GA designs (i.e., by expanding the intersection of the plasma and transiting gas), however, another key aspect of this design is that it limits the plasma interaction with the metallic electrodes and containment walls. The strategy hopes to prevent the high current density arcs typical at atmospheric pressure from repeatedly anchoring or rooting to small surface areas or spot(s). This anchoring leads to undesirable metal vaporisation and electrode erosion[31,32]. Despite limiting the plasma-wall interaction, this design characteristic cannot be eliminated due to the necessity of current transfer between the electrodes to sustain the plasma. Indeed, GA designs often rely on metallic wall interaction for enhancement via thermionic emission[33], with stationary arc configurations recently shown to favourably boost 'cost-conversion' metrics[24]. Recent reports by *Böddeker et al.*[31] have investigated the formation of plasma 'spots' resulting from material erosion and metal vaporisation in a 3D GA plasma reactor. The authors showed that plasma-wall erosion can occur even at relatively low current levels (i.e., ~0.1 A) due to the particulars of the plasma dynamics. Indeed, many laboratory scale GA designs already operate at current levels around 300 mA[23,24,34] which is above the threshold of several atmospheric plasma jet designs utilised in the deposition of metal films [35,36]. The viability of scaling the GA approach to higher power densities without significantly increasing electrode erosion therefore remains questionable. Indeed, modern day implementations of high-powered arcs at atmospheric pressure are synonymous with metallurgical applications such as welding [37-39].

In the context of NF, anchoring a relatively high current arc to a metal surface[37], even intermittently, poses a significant risk of contaminating the produced NO_x with common soil hazardous metals such as copper and chromium (i.e., stainless steel)[40]. Of course, there is also the considerable issue of severely limiting the reactor longevity due to frequent electrode damage[31,34]. Heavy metals, even in trace levels, manifest as a very damaging pollutant of soil, a non-renewable resource[41]. Effluents from arc welding are known to contain both micron and sub-micron size metal dust particulates[42-44]. Removal of metal dust from GA plasma reactors would likely require downstream filtration systems, increasing the cost and complexity of any plasma-based NF process. Cold-trapping or water washing of metallic fragments is particularly complicated by the presence of NO_2 which has a relatively high boiling point (i.e., will condense in a cold trap) and has a high affinity to hydrolyse (a fact that is exploited in producing HNO_3 from gas phase NO_x). Approaches which can sustain an electrode-free (i.e., metal free) ignition at higher powers and flow rates, where the plasma is also isolated from its containment, would therefore provide a significant advantage for plasma-based NF.

Swirling or vortex gas flows can also be employed to stabilise MW plasmas under atmospheric conditions without the need for (metallic) electrodes[45-49]. This is achieved using the unique surface wave sustained discharge mode of MW plasmas[50-52]. The latter offers a distinct advantage of the plasma being located in the vortex centre (i.e., tube centre), completely removed from interacting with the container walls, unlike typical (gliding) arc plasmas where discharge currents interact with walls and electrode materials. The surface wave mode is also inherently scalable, with ignition possible above atmospheric pressures, i.e., up to several bars[51]. Such over-pressure conditions can therefore support the high gas throughputs needed for future industrial deployment. MW plasmas have shown utility for pollution abatement[3,53,54]

including the destruction of NO_x species in gas streams[3,55-58], an application which has to-date achieved a relatively high technology readiness level[59]. The use of MW plasmas at atmospheric pressure for NO_x production rather than destruction has, however, received little scrutiny to-date. In light of recent efforts to find alternative CO_2-free means of NF, coupled with recent advances in solid state MW technology (allowing exceptional control of discharge conditions), MW-sustained plasma presents an interesting prospect for NF. The potential for an electrode-free and hence contamination-free plasma-based NO_x production process is particularly alluring given the need to avoid inadvertent impacts on soil and eco-systems, while at the same time ensuring reactor longevity.

In light of this, we report here a surface-wave sustained MW plasma in air (and N_2/O_2 mixtures at various mixing ratios) for NO_x production. We combine plasma imaging and exhaust diagnostics (measuring NO and NO_2) with quasi-1D chemical kinetics modelling, to give a detailed account of the total NO_x formation and the underlying mechanisms.

RESULTS AND DISCUSSION

The aim of our work is to discover the key conditions affecting NO_x production for an atmospheric pressure MW plasma sustained within a vortex flow in a surface wave sustained mode. This includes flow dependence, power dependence and plasma ignition with O_2-enriched air mixtures (i.e., various N_2/O_2 ratios). In **section 3.1** we present our experimental findings in terms of total NO_x production and energy cost, in **section 3.2** we provide more insight in the underlying mechanisms, based on the quasi-1D numerical analysis, while in **section 3.3** a conclusion is given.

3.1 NO_x production and energy cost

The MW surface wave mode allows relatively long plasma filaments to be maintained along the axis of a plasma tube at atmospheric pressure, where the plasma acts as one half of its own coaxial waveguide (the other side being the quartz container). In this scenario the plasma column is sustained far beyond its ignition point within a tapered waveguide (e.g., using a surfatron or surfaguide applicator[50,57]) where the applied MWs are propagated perpendicularly (relative to the ignition waveguide) along the plasma column, producing a typically warm plasma (under atmospheric pressure). Periodic exchange of the energy in the wave field heats electrons within the skin depth of the contracted plasma filament[49,60,61] where the axial extent (i.e., length) of the plasma column corresponds to the point at which the wave energy is fully absorbed.

Plasma-based conversion of inert molecules, such as N_2, provides unique reaction pathways not available in thermal conversion. Electrons cause excitation towards the lowest vibrational levels in N_2 and O_2, followed by further vibrational-vibrational (V-V) collisions, which enable a "ladder-climbing" process, gradually populating higher vibrational levels (i.e., $N_2(v)$, $O_2(v)$). Maintenance of relatively homogeneous mean electron energies near the vibrational excitation threshold of N_2 and O_2 ($\sim$1-3 eV) can therefore enable considerable energy coupling to vibrational populations in air mixtures. Vibrationally-excited molecules are however strongly affected by high gas heating, causing vibrational-translational (V-T) relaxation and destruction of vibrational species. Excessive gas temperatures should therefore be limited in order to fully exploit the benefits of vibrational excitation as most efficient gas conversion process[14,62,63]. Indeed, V-T relaxation, which depopulates the vibrational levels upon collision with ground state gas molecules, is more efficient at higher gas temperature.

The dominant chemistry for NO_x production in atmospheric pressure air plasmas proceeds via a vibrationally-enhanced Zeldovich mechanism[14,25,64] consisting of the following reactions:

$$O + N_2/N_2(v) \leftrightarrow N + NO \qquad \text{(Reaction 1)}$$

$$N + O_2/O_2(v) \leftrightarrow O + NO \qquad \text{(Reaction 2)}$$

The above two reactions are typically rate-limited by **reaction 1**. The mechanism is significantly different from the thermal Zeldovich mechanism (i.e., involving only ground state N_2 and O_2) due to the presence of vibrationally excited N_2 and O_2 molecules, uniquely available in plasmas. The vibrationally excited N_2 molecules lower the dissociation threshold required to break the strong N_2 triple bond ($\sim$10 eV) through colliding with O atoms (**reaction 1**). The N atoms formed in **reaction 1** can then further react with both ground state and vibrationally excited O_2 molecules (**reaction 2**) to produce another NO. Reaction 2 also produces an additional O atom, which can again react with ground state and vibrationally excited N_2 molecules (i.e., **reaction 1**) providing a tightly coupled reaction loop. The NO formed in both steps can be oxidised to produce NO_2 via further interaction with O atoms:

$$NO + O \rightarrow NO_2 \qquad \text{(Reaction 3)}$$

Figure 1 presents the total NO_x production and corresponding energy cost for a range of absorbed power and flow rates in our surface wave sustained atmospheric pressure MW plasma, in N_2/O_2 mixtures at different ratios. Data is collected in triplicate, with the average shown. Due to the high stability of the solid-state power supply, the variation in the collected data is found to be typically less than 3 % of the absolute NO_x concentrations, and hence error bars are not visible in **figure 1**. The absolute NO_x production in units of (normal) litres per minute along with the equivalent energy cost normalised to the inlet gas flow rate (i.e., units of MJ/L) are shown on the right-hand y-axes in **figure 1**. For the lowest air (i.e., N_2/O_2 80/20 mix) flow rates investigated, i.e., 5 L/min (see **figure 1 a**), a peak NO_x production of $\sim$4.3 % is measured at the highest absorbed MW powers (i.e., 870 W and 1.07 kW), with an energy cost in the range of 6-7 MJ/mol. In terms of absolute NO_x

production, this corresponds to a peak production of 0.22 L/min with an energy cost in the range of 0.24-0.29 MJ/L. At the lower powers (i.e., 520 W and 280 W) both energy cost and NO_x production are reduced. This is attributed to the reduced gas heating, which promotes higher vibrational populations (i.e., larger V-T non-equilibrium), yielding more energy-efficient NO_x production[14,23,24,63,65].

The relatively high energy costs found at 5 L/min (**figure 1 a**) correlate to the visual observation of a plasma filament with significant fluctuations (both radially and laterally). Excessive heating at low mass flow rates results in buoyancy-driven fluctuations (i.e., 'natural' convective cooling). The relatively low intensity of the vortex flow at this flow rate is unable to overcome, via advective cooling, the high gas heating rate typical in 'warm' contracted atmospheric pressure molecular plasmas[49,65]. Indeed, ignitions for flow rates < 5 L/min were typically too unstable and oscillatory in behaviour, so they could yield damage to the quartz tube walls.

Enriching the air feed with O_2 to near stoichiometric mixtures is known to significantly enhance NO_x production in both thermal and plasma-based processes[14,25,64]. **Figure 1 a** indeed reveals that N_2/O_2 ratios between 60/40 and 40/60 result in higher NO_x production and lower energy cost. This trend continues across all flow rates and powers shown in **figure 1**, although it is less pronounced at higher flow rates. The highest NO_x values at 5 L/min (**figure 1 a**) are found to be ~5.2 % or 0.26 L/min with an energy cost of ~4.8 MJ/mol (0.2 MJ/L) at 870 W. The observed benefits of O_2 enrichment to near-stoichiometric ratios are consistent with earlier reports in gliding arc plasmas[23,24,28]. The addition of O_2 promotes greater utilisation of the N atoms (produced in **reaction 1** of the Zeldovich mechanism) via reaction 2, and also increases the availability of O atoms for reaction with N_2 molecules (i.e., reaction 1), as discussed above; so, it enhances the overall Zeldovich mechanism.

Upon doubling the mass flow rate from 5 to 10 L/min (**figure 1 b**) we find a drop in the % NO_x produced (explained by the shorter gas residence time), but this is only marginal, while a considerable drop in the energy cost is obvious for all powers. Typical energy costs are clearly < 4 MJ/mol. The highest NO_x concentrations at 10 L/min reach ~5 % or 0.5 L/min for an energy cost of ~3.1 MJ/mol (0.13 MJ/L) in a 50/50 mix at 1.07 kW. Unlike at 5 L/min, the lowest energy cost does not correlate with the lowest power. For 520 W absorbed power we find total NO_x concentration reaching ~3.3 % (0.33 L/min) with an energy cost of 2.3 MJ/mol (0.09 MJ/L), while for 280 W a total NO_x % of ~1.7 % (0.17 L/min) requires 2.4 MJ/mol (0.1 MJ/L).

The efficiency gains found when doubling the gas flow rate (without a large drop in % NO_x production) indicate a considerable benefit in utilisation of relatively high gas flow rates and hence short gas residence times in the plasma (see explanation in **section 3.2**). Visually the plasma is found to have a more stable operation at 10 L/min compared to 5 L/min. The recorded plasma width is typically similar for increasing flow rates, and widens somewhat at higher powers. The plasma length typically increases upon increasing power (up to ~1 kW). This is consistent with the surface-wave mode behaviour[51] where MW power is absorbed as it propagates in the region between the plasma filament and the quartz tube, elongating until the wave power is fully absorbed. The plasma elongation results in longer residence times for gas species inside the plasma, however, by also increasing the gas flow rate, the overall residence time in the plasma is reduced, because the rise in flow rate is higher than the rise in plasma length upon increasing power, and we find a net benefit in terms of the energy cost.

When further doubling the mass flow rate from 10 L/min to 20 L/min (**figure 1 c**) we see again a drop in energy cost. Interestingly, the highest power (i.e., 1.07 kW) is now the most efficient condition, with the highest NO_x concentration at the lowest energy cost. This extends from the trend at lower powers for 10 L/min (see **figure 1 b**) where the most efficient conversion occurred at 520 W rather than 280 W. At an absorbed MW power of 1.07 kW, ~3.8 % total NO_x concentration is measured for a 50/50 N_2/O_2 mix, with a corresponding energy cost of ~2 MJ/mol, the lowest achieved in our study. This promising metric is exemplified by considering the absolute NO_x production achieved at ~0.77 L/min for an energy cost of ~0.08 MJ/L.

The trend in gas flow rate presented here shows a very interesting avenue to drive higher efficiencies, by increasing gas flow rate in combination with higher MW powers. This would be highly beneficial for the high throughputs required in future commercial realisation. The limited gas residence time inside the plasma likely limits back reactions of the formed NO with N (the reverse of reaction 1 above)[14]. Further discussion of the underlying reaction mechanisms is given in **section 3.2** below.

The total NO_x concentration obtained here (**figure 1**) is comparable with the best performing plasmas reported for NO_x production to-date (see **table 1** and **figure 2**), including the recent record values reported for a 3D rotating gliding arc plasma by *Jardali et al.*[24]. It must be noted that the low energy values for 1980's MW plasma shown in **table 1** and **figure 2** did not include the large energy associated with using a vacuum pump. Such energy costs in fact are comparable with the energy needed to generate the plasma in the first instance making the approach unfeasible. Our lowest energy cost of ~2 MJ/mol (**figure 1 c**) ignited with relatively high gas flow rates of 20 L/min, giving 3.8 % total NO_x concentration is, to the best of our knowledge, one of the most efficient performances for NO_x production demonstrated in plasma-based NF at atmospheric pressure to-date[5,7,10,23-25]. Indeed, the record values of *Jardali et al.*[24] for gliding arc plasma have an absolute production of ~0.11 L/min NO_x compared with ~0.77 L/min found here at our lowest energy cost of ~2 MJ/mol (~0.08 MJ/L) and highest flow rate of 20 L/min. The most promising trend observed here is therefore that future investigation of higher flow rates with higher powers could lead to further improvement on this 'conversion-cost' metric with benefits to scaling plasma-based NO_x production. Unfortunately, higher power and flow rate conditions were not possible in our current reactor configuration due to the limits of the power supply (i.e., ~1 kW) and reactor configuration (i.e., limitations of the gas connections at high flow rates and safety limitations in our current lab relating to ventilation of high NO_x levels), but this will be the subject of future work.

Despite the exciting progress to-date, plasma-based NF is currently still not competitive to the highly optimised and mature H-B process fixing > 10 % N into NH_3 for an energy cost of ~0.5 MJ/mol[6]. However, as recently underlined by *Rouwenhorst et al*.[7], a more suitable

comparison for state-of-the-art NF into NO_x would be an electrolysis-based H-B process combined with the Ostwald process (oxidising NH_3 into NO_x with eventual dissolution in water, forming HNO_3). Notably, in contrast to the traditional H-B process producing H_2 using steam reforming of methane, electrolysis-based H-B offers an environmentally benign alternative based on (water) electrolysis to produce H_2 without a CO_2 by-product. In this context the authors provide a revised target of ~0.7 MJ/mol[7] (i.e., lifting the target from ~0.5 MJ/mol of the traditional H-B process) for future plasma-based NF processes to be highly-competitive with this electrolysis-based H-B benchmark, although it must be realised that this electrolysis-based H-B process is not yet the standard in industry. Our MW discharge configuration discussed here shows much promise to achieve such a target, given its low technology readiness level at present. Critically, the results presented here show that stable plasma operation with relatively high gas throughput is possible without the filament touching its container, which contrasts to other plasma reactor configurations. Optimal conditions in gliding arc plasmas, for instance, are presently limited to relatively low mass flow rates and powers[23,24] and therefore present a considerable challenge for scale-up. The high gas throughput and production rates of MW plasmas, as demonstrated here, will offer greater flexibility for plasma-based NF, powered by intermittent renewable electricity sources such as solar and wind [7,66] while also offering a promising avenue for further reducing energy costs. The electrode-free ignition, discussed in this work, provides a significant advantage, given the reduced energy losses to the walls, which limits damage especially at higher powers, and has the key benefits of a prolonged reactor lifetime with no metal contamination (potentially detrimental to soil and ecosystems) during NO_x production.

Future avenues for reducing the energy cost of the plasma-based NF could include the use of downstream catalysts[59], particularly if they could effectively utilise the high population of vibrationally activated species and the heated gas available in the vicinity of the plasma (see **section 3.2** and **SI**, **section S.3.2**). Further, innovations to limit back reactions (which include the findings of this report) or downstream cooling of the plasma exhaust could also prove beneficial to lowering energy costs. Indeed, the absorbed energy is dissipated primarily to gas heating in the present process. Only a minority fraction of the coupled energy is converted to chemical energy due to enthalpy of formation requirements for nitrogen oxidation. The 'warm' plasma discharge provides the activation levels necessary for both thermal and (critically) vibrationally induced nitrogen oxidation. The unused vibrational populations are eventually returned as heat in the exhausted gas downstream (i.e., V-T relaxation). The theoretical "ideal value" for the chemical energy coupling in warm plasmas such as MW or GA reactors of 0.5 MJ/mol has been suggested recently by *Rouwenhorst et al [7]* (see red triangle in **figure 2**). Based on the best metrics found in this report (i.e., 3.8 % NO_x at 2 MJ/mol) this would result in circa 1.5 MJ/mol lost as heat energy. This underlines the importance of recovering heat energy as a key component to driving efficient implementation of this process. Modern waste heat recovery technologies (e.g., gas-liquid plate exchangers[67] for high grade waste heat (> 300 C) or contemporary Stirling engine designs[68] for lower grade waste heat ~50-300 C) could offer significant improvements in heat recovery compared to the state-of-the-art technologies available a century ago to Birkeland and Eyde.

As mentioned in **section 1** above, given its relatively high cost in the original B-E process the energy overhead of the NO_2 absorption stage will also need particular attention to develop the technology readiness of plasma-based NF. Modern advancements of NO_x trapping technologies commonly used in the automotive applications employing absorbents such as BaO[11,12] in combination with temperature/ pressure swing absorption techniques could be promising in this regard[7].

Although pre-compressed dry gases (Air Liquide 99.999 % purity N_2 and O_2 cylinders) are utilised in this work due to our laboratory infrastructure, on demand compression of ambient air would be a more energy-efficient supply infrastructure (notably the original B-E process used air blowers[8,69]). Tankless membrane air compressors for instances have an energy rating of about ~1 W per L/min flow rate[70]. Low-cost compressors would therefore represent a relatively small overhead compared to the MW energy input (i.e., ~300-1000 W) at typically << 5 % of the absorbed plasma power. We estimated the cost of using pre-compressed air bottles (as per our laboratory infrastructure) at several orders of magnitude higher per litre compared to the cost of using such a tankless (i.e., on demand) air compressor. Of course, integrated processes which can recirculate the compressed gas could help lower this energy overhead even more. Further to this, the use of high gas flow rates (as shown to be beneficial in this work) will not include a large energy burden compared to the cost of nitrogen oxidation in the plasma or downstream processes used to produce nitric acid.

Advancing the technology readiness of MW plasma-based NF will also depend on the architecture of power delivery. The beneficial characteristics of using solid-state MW amplifiers over magnetrons will be important in this regard. Solid state is inherently, modular in contrast to magnetrons which require large DC power supplies and enlarged magnetron cavities for scale up while the superior frequency stability and power control of solid-state amplifiers allow mixing with low losses. This modularity will be key for the 'decentralised scalability' requirements of utilising intermittent electricity powered NF processes. Further, this modular format allows low voltage (and hence low cost) DC power supplies limiting capital expenditure. Solid state amplifiers also have a considerably enhanced longevity (~x10) compared to Magnetron technology. These characteristics will enable collections of amplifiers and mixers to be deployed in flexible reactor arrangement, allowing both multiple parallel reactors and/or in smaller number of higher power plasma reactors. The efficiencies of solid-state MW power amplifiers are already typically ~50 % and are set to exceed magnetrons in the coming years (currently at ~70 % efficiency from 'plug to load'). Indeed, solid-state MW power transmission already likely supersedes low frequency ~kHz and DC powered plasma reactor designs of current research interest (e.g., GA's and dielectric barrier discharges (DBD's)) as these sources typically sacrifice a large fraction of the transmitted power in high resistance components used to ballast/stabilise the dynamic arc conditions. Current state-of-the-art solid-state high-powered MW amplifiers use laterally-diffused-metal-oxide-semiconductors (LDMOS; as employed in this report). The emergence of high-powered Gallium Nitride (GaN) amplifiers will likely drive significant efficiency improvements[71].

In order to better understand the benefits of higher flow rate on the NO_x production efficiency, presented in **section 3.1**, we applied a quasi-1D model (see **section 2.3**) to our conditions. In **figure 3** we present the simulated NO_x concentrations for an N_2/O_2 ratio of 80/20 (dry air) at 870 W and two different flow rates (10 and 20 L/min), for the feed gas passing through the plasma length (0 < x < 25 cm) and continuing 'downstream', where a steady state is eventually reached in terms of total NO_x concentration (at x > 35 cm). It must be noted that the converted mix is found to be primarily NO and NO_2 with other N_xO_y species found to be negligible in quantity. Indeed, this is consistent with our experimental findings of **section 3.1**, where NO and also NO_2 are the only measurable outputs. Notably, the ratio of NO_2 to NO will increase downstream as NO is slowly oxidised to NO_2 (i.e., as the gas cools and the relatively slow NO oxidisation reaction proceeds), however, comparison of the total NO_x at its steady state just outside the plasma region (as defined by the model) with a NDIR/UV gas sample taken downstream will be equivalent (as the total NO_x remains unchanged once a steady state is reached outside the plasma). The total NO_x concentration shown in **figure 3** (i.e., NO and NO_2) is a summation of the contributions for three sections, which simulate the gas transiting through two inner (i.e., $0 < r_1 < 2.3$ mm and $2.3 < r_2 < 3.5$ mm) and an outer region (i.e., $3.5 < r_3 < 8$ mm) of the plasma filament, centred within the gas plug inside a quartz tube of inner radius 8 mm (see **section 2.3** and **SI**, **section S.2.2** for the model details). This partition serves as a proxy to study the distribution in plasma power density that different gas molecules will 'feel' when transiting different sections of the gas plug.

Comparing the total calculated NO_x concentrations with the experiments at the same N_2/O_2 ratio (80/20), power (870 W) and flow rates, we find agreement of about ~15% between the model and experiment. Given the required assumptions of the quasi-1D modelling, this is deemed sufficient agreement to enable insight into the primary chemical trends. Indeed, to describe the detailed chemistry within reasonable calculation time, the model must simplify the physics (see **section 2.3**). In future work, it would be interesting to develop more sophisticated higher-dimensional models, to reach better agreement with experiments, but this is only feasible upon increasing computational power. At x > 35 cm in **figure 3**, corresponding to downstream the MW plasma, the simulated total NO_x concentration is ~3.9 % for 10 L/min, while our NDIR/UV analysis at the same conditions (N_2/O_2 ratio and power; **figure 1**) indicates a total NO_x concentration of ~3.6 %. Increasing the flow rate to 20 L/min, the modelling predicts a total NO_x concentration of ~2.6 %, while our experiments reveal a value of ~2.2 %. The doubling in gas flow rate from 10 L/min to 20 L/min results in a drop in the total calculated NO_x concentration by only ~33 % (i.e., from 3.9 % to 2.6 %) (**figure 3**), with a similar drop found in our experiments of ~39 % (i.e., from 3.6 % to 2.2 %). This is a reasonable quantitative agreement, given the approximations of the quasi-1D modelling, and indicates the capabilities of the model for predicting the general trends with regard to flow rate behaviour, which is of particular interest here. Similar agreement was reached at the other N_2/O_2 ratio and powers investigated in **figure 1**.

Analysis of the main production avenues for NO shows that the Zeldovich mechanism (**reactions 1** and **2** of **section 3.1**) dominates, in agreement with literature for GA plasmas[14,23,24,63,65]. At 10 L/min the thermal Zeldovich mechanism (i.e., involving ground state N_2) accounts for 28 % of NO production, while the vibrationally-enhanced Zeldovich mechanism (i.e., involving $N_2(v)$) accounts for the remaining 72 %. At 20 L/min we see a similar breakdown, with the thermal and vibrationally-enhanced Zeldovich mechanism accounting for 26 % and 74 % of NO production, respectively.

The rate-limiting step in the (vibrationally-enhanced) Zeldovich mechanism is $O + N_2/N_2(v) \leftrightarrow N + NO$ (**reaction 1** of **section 3.1**) with both $N_2(v)$ and O concentrations as potential limiting factors to NO production. The second part of the Zeldovich mechanism, i.e., $N + O_2/O_2(v) \leftrightarrow O + NO$ (**reaction 2** in **section 3.1**) involves (vibrationally excited) O_2 and N atoms (primarily produced by **reaction 1**). However, the N atoms also play a pivotal role in NO loss (back **reaction 1**)[14]. In **figure 3** we see the major contribution from the outer region of the filament ($3.5 < r_3 < 8$ mm) in terms of overall NO_x production, as this covers a much wider region (i.e., accounting for 81 % of the gas plug volume here, see **section S.2.2 in the SI**). In the following we will therefore focus on this region to gain further insight in the underlying mechanisms, given its dominance on the total NO_x produced.

In **figure 3 a,** at a flow rate of 10 L/min, we see the calculated peak NO_x concentration is reached inside the plasma region (at x~15 cm). In **figure 3 b,** at a flow rate of 20 L/min, the peak NO_x concentration shifts to the end of the plasma region (~20 cm). Notably the peak NO_x concentration reached at 20 L/min (~2.7 %) is virtually sustained outside the plasma region (to ~2.6% at steady state; x > 35 cm), while the NO_x concentration for 10 L/min falls from a peak of ~5.3 % (at ~15 cm) to ~3.9 % (x > 35 cm). This difference is attributed to the different impact of the back reactions at 10 L/min vs 20 L/min, as explained below.

The calculated total NO_x production rate in the region $3.5 < r_3 < 8$ mm is plotted in **figure 4**. At 10 L/min, the peak production (**figure 4 a**) corresponds to the sharp increase in NO_x population (seen in **figure 3 a**), for x > 10 cm. At x~12 cm, however, the NO_x production slows down and eventually turns negative (corresponding to NO_x destruction) at x~15 cm. The back reaction (reverse Zeldovich **reaction 1**) becomes dominant here, as indicated in **figure 4 a**. The comparatively longer residence time in the plasma at 10 L/min (~0.077 s) results in lowering the peak NO_x concentration due to this back reaction occurring during the gas transit through the latter half of the plasma region. In contrast at 20 L/min, as shown in **figure 4 b**, the peak production is shifted to the end of the plasma region. The shortening of the residence time (only ~0.049 s for transiting the plasma region) suppresses the back reaction, with peak NO_x values sustained as the gas leaves the discharge region. Although a higher gas flow rate leads to a drop in NO_x production, both our experimental and calculation results show a drop of only 33 (or 39) % in overall NO_x produced, despite a 100 % change in flow rate (i.e., from 10 L/min to 20 L/min). The higher gas flow rate therefore yields somewhat less conversion (for similar power conditions) but this is largely compensated by the more energy-efficient production, because of the lack of back reactions.

When comparing **figure 4 a** and **figure 4 b**, we see that the back-reactions contribute less and therefore the energy use in the reactions is more efficient at 20 L/min. It is clear that the peak NO_x production rate is lower at 20 L/min than at 10 L/min (although the peak is clearly broader, so the overall production is not so much lower, especially because no NO_x destruction occurs, as explained above). Therefore, both conditions show a similar energy cost. In addition, despite the NO_x percentage yielded being lower at the higher flow rate, the absolute production of NO_x (i.e., in L/min) is actually larger at the higher flow rate of 20 L/min. This manifests as ~0.54 L/min NO_x outflow at 20 L/min versus ~0.39 L/min NO_x at 10 L/min gas flow rate. This is consistent with the experimental trends discussed in **section 3.1** above. The lower peak production rate at 20 L/min can be explained by the lower gas temperature and vibrational temperature predicted by our model, as plotted in **figure 5**. For a flow rate of 10 L/min, a peak in calculated bulk gas temperature of ~3100 K is reached at x~15 cm (in the outer filament region $3.5 < r_3 < 8$ mm), while at 20 L/min, the calculated peak bulk gas temperature in the same outer region is only ~2500 K (see **figure 5 c**). Notably, our model predictions are not corroborated directly by experimental measurements in this report, however, the span of temperatures found here is largely in line with earlier reports using optical diagnostics[77]. Such techniques consider an accuracy of ~10-30 %[78], an uncertainty range consistent with the accuracy expectations of our simulations.

Gas temperatures in the inner regions of the plasma filament (which account for a combined 19 % of the gas plug volume and thus are not so impactful to NO_x production) are given in **figure 5 a** and **figure 5 b**. The gas temperatures are clearly higher in the inner regions, both at 10 and 20 L/min, due to the higher power density, with peak gas temperatures of ~4300 K (at 10 L/min) and ~3800 K (at 20 L/min) for $2.3 < r_2 < 3.5$ mm, and even ~6000 K (at 10 L/min) and ~5500 K (at 20 L/min) for $0 < r_1 < 2.3$ mm. Hence, at a flow rate of 20 L/min, the calculated peak bulk gas temperatures are clearly lower in all plasma regions (see **figure 5 a, b, c**). In addition, for 20 L/min the peak gas temperature is reached only near the end of the plasma region (x ~ 20 cm, while it is at x ~ 15 cm for 10 L/min). Indeed, the gas transiting the plasma region has less time to heat up within the shorter residence time. Combined with the higher advective cooling at 20 L/min, this leads to lower gas temperatures, resulting in somewhat lower NO_x production. However, as discussed above, this drop in NO_x production is compensated significantly by the absence of back reactions, leading to lower energy costs for this higher gas flow rate.

The vibrational temperature is also plotted in **figure 5**, and applies to the N_2 vibrational levels, and more specifically the population of the first vibrational level with respect to the ground state, i.e., $T_v^{(v=0 \leftarrow v=1)}$ (see **SI**, **section S.2.6**). We see that the vibrational temperature is clearly higher than the gas temperature in the first part of the plasma in all cases, indicating a strong overpopulation of the N_2 vibrational levels, or a strong vibrational-translational (V-T) non-equilibrium. It does not only apply to the first N_2 vibrational level, but also to the higher levels, as clearly observed in the calculated vibrational distribution function (VDF), plotted in the **SI**, **section S.3.4**, **figures SI.5** and **SI.6**. However, upon rising gas temperature, V-T relaxations (i.e., collisions of the vibrational levels with ground state molecules) become increasingly important, causing a drop in the vibrational level populations, and hence in the vibrational temperature, which becomes nearly equal to the gas temperature (V-T equilibrium). Hence, this means that the VDF will follow a Boltzmann distribution, dictated by the gas temperature, as is clear from the **SI**, **section S.3.4**, **figures SI.5** and **SI.6**. Nevertheless, both gas temperature and vibrational temperature rises further to a maximum around x~15 cm (at 10 L/min) or close to x~20 cm (at 20 L/min). At these high values of gas and vibrational temperature, the thermal and especially the vibrationally-enhanced Zeldovich mechanism will be very important, explaining the high NO_x production rate (before the back reaction takes over at 10 L/min). Note that in the inner filament regions, the vibrational temperature is somewhat lower than the gas temperature above x ~ 10 cm, while both temperatures are equal to each other in the outer filament region (which accounts for 81% of the volume), indicating that the vibrationally-enhanced Zeldovich mechanism will be relatively more important here.

The electron temperature, also presented in **figure 5**, is on average about 0.8 eV (~8000 K) in all plasma regions, for both 10 and 20 L/min, with a corresponding (average) reduced electric field calculated to be 22 Td (not shown), which are indeed ideal conditions for strong vibrational excitation[14]. In addition, the electron temperature is clearly higher than the gas and vibrational temperature, especially in the outer region of the filament (i.e., $3.5 < r_3 < 8$ mm) which dominates the overall NO_x production. This indicates that our MW plasma at atmospheric pressure is not a thermal but a warm plasma. In the afterglow (i.e., x > 25 cm), the electron temperature drops dramatically to very low values, due to the absence of plasma power to heat the electrons, and it approaches the gas temperature, hence the gas becomes thermalised.

Not only the N_2 molecules have a high vibrational temperature, the same is true for the O_2 molecules. Indeed, substantial populations of both $N_2(v)$ and $O_2(v)$ are predicted by the model, as shown in **figure 6** for the outer filament region. The relative population of the first N_2 vibrational level (i.e., $N_2(v=1)$) reaches peak values of 12.3 % of the gas mix at 10 L/min, and of 13.2 % at 20 L/min. Likewise, for $O_2(v=1)$ the relative population peaks at ~4 % of the total gas mix at both 10 and 20 L/min, with an associated peak vibrational temperature $T_v^{(0 \leftarrow 1)}$ of 1700 K. The entire vibrational distribution function for both O_2 and N_2, at both 10 and 20 L/min and various positions in the plasma, is given in the **SI** (**figure SI.5** and **figure SI.6**). The higher N_2 and O_2 vibrational levels have somewhat lower populations, as indicated in **figure 6** for $N_2(v=5)$ and $O_2(v=5)$, and they also drop faster in the afterglow. When comparing 10 and 20 L/min (**figure 6 a** and **b**), we see that the N_2 and O_2 vibrational populations are retained over a longer distance at 20 L/min than at 10 L/min. This is due to the shorter residence time when doubling the mass flow rate, leading to faster mass transport of the vibrationally excited species. This promotes the forward reactions of the Zeldovich mechanism (**reactions 1** and **2**) with respect to the back reactions, explaining the more energy-efficient NO_x production at 20 L/min.

In **figure 7** we plot the calculated densities of O and N atoms, and of the electrons, for the outer filament region, throughout the plasma and afterglow. For 10 L/min, in **figure 7 a**, the O concentration inside the plasma region is found (on average) to be ~0.2 % of the total gas mixture, with peak values reaching ~1.6 % in the latter half of the plasma region. This is much lower than the $N_2(v)$ levels, indicating that the

O atoms are the limiting factor in the first step of the Zeldovich mechanism (**reaction 1** in **section 3.1**). Examination of the fundamental production avenues for O atoms (i.e., excluding **reactions 1-3**, which by oxidation of N_2 result in a net loss for O), we find that 67 % of the production is due to dissociation of vibrationally excited O_2 (up to v=15), upon collision with gas molecules: $O_2(v) + N_2/O_2 + \Delta H \rightarrow O + O + N_2/O_2$. Dissociation of $O_2/O_2(v)$ by electronically excited N_2 molecules (primarily $N_2(B^3\Pi_g)$ and the metastable $N_2(A^3\Sigma_u^+)$) contributes for 23 %, while direct electron impact dissociation of $O_2/O_2(v)$ accounts for just ~6%.

At 20 L/min, as shown in **figure 7 b**, the calculated O atom concentration is on average ~0.03 % of the mix, with a peak of only ~0.25 %. The reason is the more efficient O atom consumption, in the Zeldovich mechanism (forward **reaction 1**, as the back **reaction 1** is suppressed at 20 L/min) and in oxidation of NO to NO_2 (**reaction 3**), as well as the more limited O atom production due to the shorter residence time in the plasma (see below). However, despite the lower O atom concentration, the drop in overall NO_x production is limited, exactly due to the absence of the back reactions, as discussed above. At 20 L/min, the production of O atoms is found to be dominated by electronically excited N_2 molecules (i.e., $N_2(B^3\Pi_g)$ and $N_2(A^3\Sigma_u^+)$) colliding with $O_2/O_2(v)$, accounting for ~76 % of the overall O atom production, while the reaction of vibrationally excited $O_2(v)$ (i.e., $O_2(v) + N_2/O_2 + \Delta H \rightarrow O + O + N_2/O_2$) which dominated at 10 L/min, contributes only for 6 % at 20 L/min. This shift in O atom production chemistry from 10 to 20 L/min is due to the more limited time for vibrational excitation of $O_2(v)$ (i.e., V-V interactions), due to the shorter residence time in the plasma at 20 L/min. This is clear from the O_2 VDF plotted in the **SI**, **section S.3.4.** Indeed, in **figure SI.6** we see the relative underpopulation of $O_2(v)$ at 20 L/min compared to 10 L/min. This shift in chemistry also explains the overall lower O atom concentration. Methods (e.g., gas quenching[79]) which can promote higher electronic N_2 excitation or higher vibrational excitation of O_2 under high flow conditions would enhance O atom formation, and could therefore provide potential avenues to further increase NO_x production at lower energy costs.

The average N atom concentration at 10 L/min (also shown in **figure 7 a**), taken over the plasma region (i.e., 0-25 cm), is found to be only ~14 ppm of the gas mix, with the production trend following the NO_x production. The relatively low N atom concentration is due to the tightly coupled Zeldovich mechanism (**reaction 1** and **2**), where the N atoms play an intermediate role and thus have a short lifetime. Surplus N atoms, however, play a key role in limiting NO formation, due to the back reaction: $N + NO \rightarrow O + N_2/N_2(v)$ (i.e., back of **reaction 1**). At 20 L/min, the N atom concentration in the plasma is found to be further reduced to ~1.2 ppm (on average), as shown in **figure 7 b**. This very low N atom concentrations is consistent with the limited back reaction at 20 L/min, as discussed above (see **figure 4 b** above).

Electrons do not play a direct role in NO production (cf. Zeldovich mechanism), but are essential in activating the gas initially, and sustaining the chemistry, mainly by electron impact vibrational excitation of N_2 and O_2. The electron density inside the plasma reaches a peak of ~3×10^{11} cm^{-3} at 10 L/min and of ~1×10^{11} cm^{-3} at 20 L/min (see **figure 7**). This has however no real impact on the NO_x production.

Future numerical investigations would undoubtedly benefit from a more spatially resolved description of the plasma dynamics and chemistry. A necessary prerequisite for this would be the investigation of dominate pathways in fully resolved approaches such as employed in this work in combination with appropriate sensitivity analysis[80] to enable a smaller subset chemistry to be derived. Such a reduced chemistry could then allow tractable plasma fluid and computational fluid dynamics studies. The large chemistry of N_2/O_2 employed in this work is largely a result of the resolution of vibrational levels. Reduction of the plasma chemistry for higher dimensional modelling will therefore need to verify which vibrational levels can be omitted or assumed via a pre-defined distribution (e.g., Boltzmann or Treanor[81]) while maintaining the required level of detail.

3.3 Conclusion

In this paper we demonstrate energy-efficient NO_x formation from air and N_2/O_2 mixtures, in a plasma filament isolated at the centre of a MW plasma tube, using a vortex gas flow. The electrode-free ignition provides a significant advantage, given the reduced energy losses to the walls, which limits damage especially at higher powers, with key benefits of a prolonged reactor lifetime and no metal contamination (which is potentially detrimental to soil and ecosystems for applications in agriculture). NO_x production is found to scale efficiently with gas flow rate and power. For relatively high flow rates (i.e., 20 L/min), increasing MW power (up to ~1 kW) leads to the highest NO_x production (~ 3.8 %) as well as minimum energy cost (~2 MJ/mol), giving the best cost-conversion metric for this work. This energy cost is the lowest reported up to now in literature for atmospheric pressure plasmas. The rising trend with power and flow rate is very beneficial, given the high-volume throughputs required for future industry deployment. Ignition in O_2-enriched air feeds close to stoichiometric N_2/O_2 ratios (i.e., 50/50) is found to benefit NO_x production, reducing energy costs.

Our numerical model offers insight into the fundamental behaviour with changing gas flow rate and residence time within the plasma. Doubling the gas flow rate limits the back reactions in the last part of the plasma, due to the shorter gas residence time. At the higher gas flow rate, sufficiently high vibrational level populations and atomic species densities are retained over a longer distance in the plasma, thus promoting the forward reactions of the Zeldovich mechanism. This leads to a comparatively small drop in NO_x production upon increasing the gas flow rate, despite the shorter residence time, and at a significantly lower energy cost.

Altogether our findings demonstrate the benefits of high flow rates (i.e., limited residence time) matched with appropriate power, for energy-efficient NO$_x$ production in atmospheric pressure MW air plasma, in a surface wave sustained mode without electrodes. Future work can consider even higher power and flow combinations to drive efficient conversion for industrial exploitation. Our work underlines the importance of residence time to prevent back reactions, gained at higher flow rates and powers. It also encourages the potential merits of other methods with great potential for reducing back reactions, discussed recently in particular for the related field of plasma-based CO$_2$ conversion[82]. This includes exhaust gas quenching using nozzles (e.g., Laval nozzle [45]) and using heat exchangers or external coolants [79] in the immediate vicinity of the plasma.

EXPERIMENTAL PROCEDURES

2.1 Resource availability

2.1.1 Lead contact

Further information and requests for resources and materials should be directed to and will be fulfilled by the lead contact, Seán Kelly (sean.kelly@uantwerpen.be).

2.1.2 Materials availability

This study did not generate new unique materials.

2.1.3 Data and code availability

Data from this study are available from the lead contact upon reasonable request.

2.2 MW plasma reactor and exhaust diagnostics

The experimental layout is schematically shown in **figure 8**. An electronic image of the setup is shown in **SI**, **section S.3.1**, along with an accompany video showing the reactor operation available for download in the supporting information. It is based on a solid-state 2.45 GHz microwave (MW) power source composed of a collection of laterally diffused metal oxide semiconductor (LDMOS) power amplifiers from which the output powers are combined in a waveguide (WR340). This waveguide is connected via an isolator and an auto-tuner to a tapered waveguide section, including a 16 mm inner diameter quartz tube. The latter is mounted perpendicularly through an 18 mm coupling hole (i.e., < 1/4 wavelength in diameter), where the plasma ignition takes place. An auto-tuner, impedance analyser and adjustable short are used to tune the electric field to optimal conditions for electrical breakdown, and to sustain a continuously powered plasma with minimum reflected power (<< 5 %). Measurement of the absorbed plasma power, a key variable, is carried out using the HOMER series auto tuner from S-TEAM labs[83] using a six-port-reflectometer (SPR) method[84]. Tangential gas injection ports coupled with a helical insert allow a swirl or vortex flow within the quartz discharge tube. Upon ignition, a surface wave sustained mode[50] is generated, with the plasma filament located at the tube centre (see inset in **figure 8**). This provides a key benefit by isolating the warm plasma from the quartz tube walls, allowing for elongated plasma column formation along the tube lateral axis.

The oxidation of nitrogen results in the production of gaseous NO and NO$_2$ via the overall reactions

$$O_2(g) + N_2(g) + 180.5 \text{ kJ/mol} \rightarrow 2NO \qquad \text{(Reaction 4)}$$

$$2\,O_2(g) + N_2 + 66.36 \text{ kJ/mol} \rightarrow 2NO_2 \qquad \text{(Reaction 5)}$$
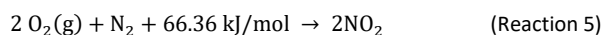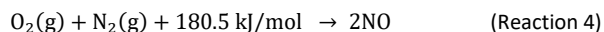
Analysis of the exhausted NO$_x$ species (i.e., NO and NO$_2$) is performed using infra-red and ultra-violet absorption spectrometry (Rosemount X-STREAM XEGP Continuous Gas Analyzer[85]), as explained in detail in the **SI**, **section S.1**. Sampling is performed once the reactor has reached a steady state in terms of the exhaust temperature as explained in **SI**, **section S.3.2**. The energy cost of the conversion from air or N$_2$/O$_2$ mixtures is obtained from the measured absorbed power and total % NO$_x$ produced (i.e., the sum of NO and NO$_2$) from the NDIR/UV as:

$$\text{Energy cost [MJ mol}^{-1}] = 10^{-6} * \frac{P\,[J\,s^{-1}] * 24.05\,[L\,mol^{-1}] * 60\,[s/min]\,] * 100\,[\%]}{\text{total NO}_x\,[\%] * \text{Flow rate [nL/min]}} \qquad (1)$$

Where P [W or J/s] is the absorbed MW power and 24.05 [L/mol] represents the molar volume of ideal gas at normal temperature and pressure conditions for which our mass flow controllers (Bronkhorst) are calibrated. The NDIR/UV data used in **figure 1** along with a breakdown for the NO and NO_2 populations has been added to the supporting information in **SI**, **section S.3.3**, **table SI.2**.

2.3 Quasi-1D chemical kinetics modelling

A quasi-1D model is employed using ZDPlasKin (Zero-Dimensional Plasma Kinetics) solver[86-88]. An overview of the simulation scheme is given in **figure 9**. The time-evolution of the species densities, including electrons, and various charged and neutral species, is calculated by considering the production and loss terms by chemical reactions:

$$\frac{dn_i}{dt} = \sum_j \left(a_{ij}^R - a_{ij}^L \right) . R_j \qquad (2)$$

$$a_A A + a_B B \,(+\Delta H) \xrightarrow{k_j} a_c C + a_D D \,(+\Delta H) \qquad (3)$$
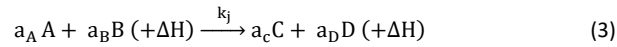
$$R_j = k_j \prod_l n_l^L \qquad (4)$$

Here n_i represents the density of species i and a_{ij}^R and a_{ij}^L are the stoichiometric coefficients of species i on the right-hand and left-hand side of reaction j. Reactions have the general form of **equation 3** where A, B, C and D are the species and a_A, a_B, a_c, and a_D their stoichiometric coefficients. ΔH in **equation 3** represents the possible energy change during the reaction. The reaction rate R_j is calculated by **equation 4**, where k_j is the reaction rate coefficient of reaction j and $\prod_l n_l^L$ represents the product over left-hand side reactants. At each time step the relation $dx = v\,dt$ advances the gas plug, so that the time-dependency is translated into an axial spatial dependency (so-called 'quasi-1D'). This assumes the velocity v is uniform across the tube diameter. Dynamic changes in the gas velocity due to temperature and stoichiometric changes in the gas mixture are updated on each time step (further details in **SI, section S.2.1** and **figure SI.1**).

The reduced electric field E/N, where N is the neutral gas density, is calculated from a specified power density.

$$E/N = \frac{\sqrt{P/\sigma}}{N} \qquad (5)$$

Here σ is the plasma conductivity, which is calculated using the electron mobility μ_e (E/N) (output from the Boltzmann solver[86,88]) via $\sigma = en_e\mu_e$ where e is the electron charge.

The power density P $[\frac{W}{cm^3}]$ is derived from experimental measurements of the absorbed power (i.e., forward minus reflected power) combined with approximation of the plasma volume via camera imaging inside the tapered section of the waveguide (see **figure 8 inset**) and visual estimation of the plasma length. A cylindrical shape is assumed for the plasma volume[63]. This is consistent with vortex stabilised discharges where the plasma is contained within the tube inner region, separated from the containment walls by a swirling or vortex flow boundary. The plasma elongates along the direction of the flow (i.e., along the axial extent of the reactor tube) forming a cylindrical shape in its steady state[48,49,63]. The light emission across the radial extent of the plasma filament (shown in **figure 8**) is used as a proxy for the plasma width. We solve the quasi-1D model for different radial positions, as explained in the **SI**, **section S.2.2**. For each of these quasi-1D models a triangular distribution of power density in the lateral extent of the plasma (i.e., along the direction of gas flow) is assumed, in line with earlier modelling of power dissipation in surface wave sustained MW plasmas[13,52]. Further details of the power density determination are given in the **SI**, **section S.2.2** and **figure SI.2**.

Next to the species densities, also the gas temperature is solved in the model at each time step, based on gas heating due to elastic collisions of electrons with the gas molecules, the enthalpy contributions from the chemical reactions between all plasma species (ΔH in **equation 3** above), heat losses to the walls and the dynamic heat capacity taking account of the gas mixture. The radially averaged gas temperature T_g (which is assumed to have a parabolic profile) is calculated by considering the time-dependent gas thermal balance equation under isobaric conditions[89,90] as:

$$N \frac{\gamma k_B}{\gamma - 1} \frac{dT_{gas}}{dt} = P_{el} + \sum_j R_j \Delta H_j - Nu \frac{\lambda}{R^2} (T_g - T_w) \qquad (6)$$

Where γ is the specific heat ratio (i.e., the ratio of the isobaric and isochoric heat capacity[63], which is function of temperature and employs data from[91]), k_B is the Boltzmann constant, P_{el} is the power density due to elastic collisions of electrons with heavy neutrals (an output from the Boltzmann solver[86,88]), R_j is the rate of reaction j with associated enthalpy contribution of ΔH_j, λ is the gas thermal conductivity, T_w is the wall temperature (set to 300 K), and R is the reactor inner radius (taken from the experiments; see **section 2.2**). It must be noted that in **equation 6** (LHS) the fluid-related term "$\gamma k_B / (\gamma - 1) dT_{gas}/dt$" is equivalent to a "$NC_p dT_{gas}/dt$" formulation, given by $\gamma = C_p/C_v$. The ratio γ is dynamically updated throughout the (isobaric) simulation based on the changing gas mixture during conversion. Finally, the non-dimensional quantity 'Nu' in **equation 6** is the Nusselt number, which is defined as the ratio of convective to conductive heat transfer to the tube walls (further details in **SI**, **section S.2.3**). The mixture fraction along with the gas temperature and the reduced electric field are continually updated in calls to BOLSIG+ as shown in **figure 9** (further details in **SI**, **section S.2.1** and **S.2.4**).

The air chemistry (i.e., N_2/O_2) employed here is detailed in our previous work[14,63,65]. 82 species are included in the model, i.e., the electrons, N_2 and O_2 molecules in ground state and various (vibrational and electronic) excited levels, various radicals and ions, as detailed in the **SI**, **section S.2.5**. For the heavy particle reactions, the rate coefficients are adopted from earlier work[14,63,92], whereas the rate coefficients for the electron impact reactions are calculated using the Boltzmann solver BOLSIG+[88] built in ZDPlasKin, as explained in the **SI**, **section S.2.4**.

SUPPLEMENTAL INFORMATION
Document '**Supp_info.pdf**' is the main supplemental PDF.

SUPPLEMENTAL VIDEO
A video '**Video S1. Microwave Air plasma operation.mp4**' of the MW reactor operating with Air at 10 L/min and absorbed power of 870 W.

AUTHOR CONTRIBUTIONS
S.K. conducted the experiments and modelling; S.K. and A.B. wrote the paper.

DECLARATION OF INTERESTS
The authors declare no competing interests.

REFERENCES
1. Snoeckx, R., and Bogaerts, A. (2017). Plasma technology - a novel solution for CO2 conversion? Chem Soc Rev *46*, 5805-5863. 10.1039/c6cs00066e.
2. Winter, L.R., and Chen, J.G. (2021). N$_2$ Fixation by Plasma-Activated Processes. Joule *5*, 300-315. 10.1016/j.joule.2020.11.009.
3. Brandenburg, R., Bogaerts, A., Bongers, W., Fridman, A., Fridman, G., Locke, B.R., Miller, V., Reuter, S., Schiorlin, M., Verreycken, T., and Ostrikov, K. (2018). White paper on the future of plasma science in environment, for gas conversion and agriculture. Plasma Processes and Polymers *16*, 1700238. 10.1002/ppap.201700238.
4. European Commission 2050 low-carbon economy roadmap. https://ec.europa.eu/clima/sites/clima/files/2050_roadmap_en.pdf. (2020).
5. Patil, B.S., Wang, Q., Hessel, V., and Lang, J. (2015). Plasma N2-fixation: 1900–2014. Catalysis Today *256*, 49-66. 10.1016/j.cattod.2015.05.005.

6. Reuvers, J.G., Brightling, J.R., and Sheldon, D.T. (2014). Ammonia technology development from Haber-Bosch to current times. International Fertiliser Society.

7. Rouwenhorst, K., Jardali, F., Bogaerts, A., and Lefferts, L. (2021). From the Birkeland-Eyde process towards energy-efficient plasma-based NOX synthesis: A techno-economic analysis. Energy & Environmental Science *14*, 2520-2534. 10.1039/d0ee03763j.

8. Birkeland, K. (1906). On the oxidation of atmospheric nitrogen in electric arcs. Transactions of the Faraday Society *2*, 98-116. 10.1039/TF9060200098.

9. Cherkasov, N., Ibhadon, A.O., and Fitzpatrick, P. (2015). A review of the existing and alternative methods for greener nitrogen fixation. Chemical Engineering and Processing: Process Intensification *90*, 24-33. https://doi.org/10.1016/j.cep.2015.02.004.

10. Eyde, H.S. (1909). The Manufacture of nitrates from atmosphere by the electric arc - Birkeland-Eyde Process. Journal of the Royal Society of Arts *57*, 568-576.

11. Schmitz, P.J., and Baird, R.J. (2002). NO and NO2 Adsorption on Barium Oxide: Model Study of the Trapping Stage of NOx Conversion via Lean NOx Traps. The Journal of Physical Chemistry B *106*, 4172-4180. 10.1021/jp0133992.

12. Fridell, E., Skoglundh, M., Westerberg, B., Johansson, S., and Smedler, G. (1999). NOxStorage in Barium-Containing Catalysts. Journal of Catalysis *183*, 196-209. https://doi.org/10.1006/jcat.1999.2415.

13. Berthelot, A., and Bogaerts, A. (2017). Modeling of CO2 Splitting in a Microwave Plasma: How to Improve the Conversion and Energy Efficiency. The Journal of Physical Chemistry C *121*, 8236-8251. 10.1021/acs.jpcc.6b12840.

14. Wang, W., Patil, B., Heijkers, S., Hessel, V., and Bogaerts, A. (2017). Nitrogen Fixation by Gliding Arc Plasma: Better Insight by Chemical Kinetics Modelling. ChemSusChem *10*, 2145-2157. 10.1002/cssc.201700095.

15. Fridman, A. (2008). Plasma Chemistry (Cambridge University Press). 10.1017/cbo9780511546075.

16. Asisov, R.I., Givotov, V. K., Rusanov, V. D., Fridman, A. (1980). High Energy Chemistry (Khimia Vysokikh Energij, Sov. Phys. *14*, 366.

17. Welch crv4 Pro rotary vane vacuum pump, user manual. https://www.welchvacuum.com/en-us/rotary-vane-pumps/rotary-vane-pump-crv-pro-4. (2021).

18. Patel, H., Sharma, R.K., Kyriakou, V., Pandiyan, A., Welzel, S., van de Sanden, M.C.M., and Tsampas, M.N. (2019). Plasma-Activated Electrolysis for Cogeneration of Nitric Oxide and Hydrogen from Water and Nitrogen. ACS Energy Letters *4*, 2091-2095. 10.1021/acsenergylett.9b01517.

19. Gorbanev, Y., Vervloessem, E., Nikiforov, A., and Bogaerts, A. (2020). Nitrogen Fixation with Water Vapor by Nonequilibrium Plasma: toward Sustainable Ammonia Production. ACS Sustainable Chemistry & Engineering *8*, 2996-3004. 10.1021/acssuschemeng.9b07849.

20. Peng, P., Chen, P., Addy, M., Cheng, Y., Zhang, Y., Anderson, E., Zhou, N., Schiappacasse, C., Hatzenbeller, R., Fan, L., et al. (2018). In situ plasma-assisted atmospheric nitrogen fixation using water and spray-type jet plasma. Chem Commun (Camb) *54*, 2886-2889. 10.1039/c8cc00697k.

21. van 't Veer, K., Reniers, F., and Bogaerts, A. (2020). Zero-dimensional modeling of unpacked and packed bed dielectric barrier discharges: the role of vibrational kinetics in ammonia synthesis. Plasma Sources Science and Technology *29*, 045020. 10.1088/1361-6595/ab7a8a.

22. Kim, T., Song, S., Kim, J., and Iwasaki, R. (2010). Formation of NOxfrom Air and N2/O2Mixtures Using a Nonthermal Microwave Plasma System. Japanese Journal of Applied Physics *49*, 126201. 10.1143/jjap.49.126201.

23. Vervloessem, E., Aghaei, M., Jardali, F., Hafezkhiabani, N., and Bogaerts, A. (2020). Plasma-Based N2 Fixation into NOx: Insights from Modeling toward Optimum Yields and Energy Costs in a Gliding Arc Plasmatron. ACS Sustainable Chemistry & Engineering *8*, 9711-9720. 10.1021/acssuschemeng.0c01815.

24. Jardali, F., Van Alphen, S., Creel, J., Ahmadi Eshtehardi, H., Axelsson, M., Ingels, R., Snyders, R., and Bogaerts, A. (2021). NOx production in a rotating gliding arc plasma: potential avenue for sustainable nitrogen fixation. Green Chemistry *23*, 1748-1757. 10.1039/d0gc03521a.

25. Patil, B.S., Rovira Palau, J., Hessel, V., Lang, J., and Wang, Q. (2015). Plasma Nitrogen Oxides Synthesis in a Milli-Scale Gliding Arc Reactor: Investigating the Electrical and Process Parameters. Plasma Chemistry and Plasma Processing *36*, 241-257. 10.1007/s11090-015-9671-4.

26. Fridman, A., Nester, S., Kennedy, L.A., Saveliev, A., and Mutaf-Yardimci, O. (1999). Gliding arc gas discharge. Progress in energy and combustion science *25*, 211-231.

27. Czernichowski, A. (1994). Gliding arc: applications to engineering and environment control. Pure and Applied Chemistry *66*, 1301-1310.

28. Van Alphen, S., Jardali, F., Creel, J., Trenchev, G., Snyders, R., and Bogaerts, A. (2021). Sustainable gas conversion by gliding arc plasmas: a new modelling approach for reactor design improvement. Sustainable Energy & Fuels *5*, 1786-1800. 10.1039/D0SE01782E.

29. Nunnally, T., Gutsol, K., Rabinovich, A., Fridman, A., Gutsol, A., and Kemoun, A. (2011). Dissociation of CO2in a low current gliding arc plasmatron. Journal of Physics D: Applied Physics *44*, 274009. 10.1088/0022-3727/44/27/274009.

30. Zhang, H., Zhu, F., Tu, X., Bo, Z., Cen, K., and Li, X. (2016). Characteristics of Atmospheric Pressure Rotating Gliding Arc Plasmas. Plasma Science and Technology *18*, 473-477. 10.1088/1009-0630/18/5/05.

31. Böddeker, S., Bracht, V., Hermanns, P., Gröger, S., Kogelheide, F., Bibinov, N., and Awakowicz, P. (2020). Anode spots of low current gliding arc plasmatron. Plasma Sources Science and Technology *29*, 08LT01. 10.1088/1361-6595/aba6a4.

32. Ramakers, M., Medrano, J.A., Trenchev, G., Gallucci, F., and Bogaerts, A. (2017). Revealing the arc dynamics in a gliding arc plasmatron: a better insight to improve CO2conversion. Plasma Sources Science and Technology *26*, 125002. 10.1088/1361-6595/aa9531.

33. Benilov, M.S. (2008). Understanding and modelling plasma–electrode interaction in high-pressure arc discharges: a review. Journal of Physics D: Applied Physics *41*, 144001. 10.1088/0022-3727/41/14/144001.

34. Ramakers, M., Trenchev, G., Heijkers, S., Wang, W., and Bogaerts, A. (2017). Gliding Arc Plasmatron: Providing an Alternative Method for Carbon Dioxide Conversion. ChemSusChem *10*, 2642-2652. 10.1002/cssc.201700589.

35. Kredl, J., Kolb, J.F., Schnabel, U., Polak, M., Weltmann, K.-D., and Fricke, K. (2016). Deposition of Antimicrobial Copper-Rich Coatings on Polymers by Atmospheric Pressure Jet Plasmas. Materials (Basel) *9*, 274. 10.3390/ma9040274.

36. Kredl, J., Drache, S., Quade, A., Polak, M., Müller, S., Peglow, S., Hippler, R., and Kolb, J.F. (2014). DC Operated Air Plasma Jet for Antimicrobial Copper Coatings on Temperature Labile Surfaces. IEEE Transactions on Plasma Science *42*, 2756-2757. 10.1109/TPS.2014.2325956.

37. Murphy, A.B. (2010). The effects of metal vapour in arc welding. Journal of Physics D: Applied Physics *43*, 434001. 10.1088/0022-3727/43/43/434001.

38. Scan arc AB plasma systems. https://scanarc.se/applications/. (2021).

39. Murphy, A.B., Tanaka, M., Yamamoto, K., Tashiro, S., Sato, T., and Lowke, J.J. (2009). Modelling of thermal plasmas for arc welding: the role of the shielding gas properties and of metal vapour. Journal of Physics D: Applied Physics *42*, 194006. 10.1088/0022-3727/42/19/194006.

40. Vodyanitskii, Y.N. (2016). Standards for the contents of heavy metals in soils of some states. Annals of Agrarian Science *14*, 257-263. https://doi.org/10.1016/j.aasci.2016.08.011.

41. Hou, D., O'Connor, D., Igalavithana, A.D., Alessi, D.S., Luo, J., Tsang, D.C.W., Sparks, D.L., Yamauchi, Y., Rinklebe, J., and Ok, Y.S. (2020). Metal contamination and bioremediation of agricultural soils for food safety and sustainability. Nature Reviews Earth & Environment *1*, 366-381. 10.1038/s43017-020-0061-y.

42. Shigeta, M., Tanaka, M., and Ghedini, E. (2019). Numerical Analysis of the Correlation between Arc Plasma Fluctuation and Nanoparticle Growth-Transport under Atmospheric Pressure. Nanomaterials (Basel) *9*, 1736. 10.3390/nano9121736.

43. Parada, J., Rubilar, O., Fernández-Baldo, M.A., Bertolino, F.A., Durán, N., Seabra, A.B., and Tortella, G.R. (2019). The nanotechnology among US: are metal and metal oxides nanoparticles a nano or mega risk for soil microbial communities? Critical Reviews in Biotechnology *39*, 157-172. 10.1080/07388551.2018.1523865.

44. Zhang, M., Jian, L., Bin, P., Xing, M., Lou, J., Cong, L., and Zou, H. (2013). Workplace exposure to nanoparticles from gas metal arc welding process. Journal of Nanoparticle Research *15*, 2016. 10.1007/s11051-013-2016-4.

45. Bongers, W., Bouwmeester, H., Wolf, B., Peeters, F., Welzel, S., van den Bekerom, D., den Harder, N., Goede, A., Graswinckel, M., Groen, P.W., et al. (2017). Plasma-driven dissociation of CO2 for fuel synthesis. Plasma Processes and Polymers *14*, 1600126. 10.1002/ppap.201600126.

46. Belov, I., Vermeiren, V., Paulussen, S., and Bogaerts, A. (2018). Carbon dioxide dissociation in a microwave plasma reactor operating in a wide pressure range and different gas inlet configurations. Journal of CO2 Utilization *24*, 386-397. 10.1016/j.jcou.2017.12.009.

47. den Harder, N., van den Bekerom, D.C.M., Al, R.S., Graswinckel, M.F., Palomares, J.M., Peeters, F.J.J., Ponduri, S., Minea, T., Bongers, W.A., van de Sanden, M.C.M., and van Rooij, G.J. (2017). Homogeneous CO2conversion by microwave plasma: Wave propagation and diagnostics. Plasma Processes and Polymers *14*, 1600120. 10.1002/ppap.201600120.

48. Wolf, A.J., Righart, T.W.H., Peeters, F.J.J., Bongers, W.A., and van de Sanden, M.C.M. (2020). Implications of thermo-chemical instability on the contracted modes in CO2 microwave plasmas. Plasma Sources Science and Technology *29*, 025005. 10.1088/1361-6595/ab5eca.

49. Wolf, A.J., Righart, T.W.H., Peeters, F.J.J., Groen, P.W.C., van de Sanden, M.C.M., and Bongers, W.A. (2019). Characterization of CO2 microwave plasma based on the phenomenon of skin-depth-limited contraction. Plasma Sources Science and Technology *28*, 115022. 10.1088/1361-6595/ab4e61.

50. Moisan, M., Ferreira, C.M., Hajlaoui, Y., Henry, D., Hubert, J., Pantel, R., Ricard, A., and Zakrzewski, Z. (1982). Properties and applications of surface wave produced plasmas. Revue de Physique Appliquée *17*, 707-727. 10.1051/rphysap:019820017011070700.

51. Moisan, M., and Pelletier, J. (2006). Physics of collisional plasmas. Application to high frequency discharges; Physique des plasmas collisionnels. Application aux decharges haute frequence (EDP Sciences, Les Ulis (France)).

52. Schlüter, H., and Shivarova, A. (2007). Travelling-wave-sustained discharges. Physics Reports *443*, 121-255.

53. Wofford, B.A., Jackson, M.W., Hartz, C., and Bevan, J.W. (1999). Surface Wave Plasma Abatement of CHF3 and CF4 Containing Semiconductor Process Emissions. Environmental Science & Technology *33*, 1892-1897. 10.1021/es9805472.

54. Marotta, E., Schiorlin, M., Rea, M., and Paradisi, C. (2010). Products and mechanisms of the oxidation of organic compounds in atmospheric air plasmas. Journal of Physics D: Applied Physics *43*, 124011. 10.1088/0022-3727/43/12/124011.

55. Baeva, M., Gier, H., Pott, A., Uhlenbusch, J., Höschele, J., and Steinwandel, J. (2002). Pulsed microwave discharge at atmospheric pressure for NOxdecomposition. Plasma Sources Science and Technology *11*, 1-9. 10.1088/0963-0252/11/1/301.

56. Balachandran, W., First, P., Manivannan, N., Beleca, R., and Abbod, M. (2015). Reduction of NOx and PM in marine diesel engine exhaust gas using microwave plasma. Journal of Physics: Conference Series *646*, 012053. 10.1088/1742-6596/646/1/012053.

57. Ferreira, C.M., and Moisan, M. (2013). Microwave Discharges: Fundamentals and Applications (Springer US).

58. Ronny, B., Hana, B., Ladislav, B., Andrzej, G.C., Miroslaw, D., Helge, G., Marcin, H., Indrek, J.g., Matti, L., Jerzy, M., et al. (2011). Plasma-Based Depollution of Exhausts: Principles, State of the Art and Future Prospects. 10.5772/20351.

59. Bogaerts, A., Tu, X., Whitehead, J.C., Centi, G., Lefferts, L., Guaitella, O., Azzolina-Jury, F., Kim, H.-H., Murphy, A.B., Schneider, W.F., et al. (2020). The 2020 plasma catalysis roadmap. Journal of Physics D: Applied Physics *53*, 443001. 10.1088/1361-6463/ab9048.

60. Castanos Martinez, E., Kabouzi, Y., Makasheva, K., and Moisan, M. (2004). Modeling of microwave-sustained plasmas at atmospheric pressure with application to discharge contraction. Phys Rev E Stat Nonlin Soft Matter Phys *70*, 066405. 10.1103/PhysRevE.70.066405.

61. Kabouzi, Y., Calzada, M.D., Moisan, M., Tran, K.C., and Trassy, C. (2002). Radial contraction of microwave-sustained plasma columns at atmospheric pressure. Journal of Applied Physics *91*, 1008-1019. 10.1063/1.1425078.

62. Bogaerts, A., and Neyts, E.C. (2018). Plasma Technology: An Emerging Technology for Energy Storage. ACS Energy Letters *3*, 1013-1027. 10.1021/acsenergylett.8b00184.

63. Van Alphen, S., Vermeiren, V., Butterworth, T., van den Bekerom, D.C.M., van Rooij, G.J., and Bogaerts, A. (2019). Power Pulsing To Maximize Vibrational Excitation Efficiency in N2 Microwave Plasma: A Combined Experimental and Computational Study. The Journal of Physical Chemistry C *124*, 1765-1779. 10.1021/acs.jpcc.9b06053.

64. Rashid Alievich, S. (2014). Selected Works of Yakov Borisovich Zeldovich, Volume I. In 26. Oxidation of Nitrogen in Combustion and Explosions, S. Rashid Alievich, ed. (Princeton University Press), pp. 404-410. doi:10.1515/9781400862979.404.

65. Kelly, S., Van de Steeg, A., Hughes, A., J. Van Rooij, G., and Bogaerts, A. (2021). Thermal instability and volume contraction in a pulsed microwave N2 plasma at sub-atmospheric pressure. Plasma Sources Science and Technology *0963-0252*. 10.1088/1361-6595.

66. Torabi, R., Gomes, A., and Morgado-Dias, F. (2018). The Duck Curve Characteristic and Storage Requirements for Greening the Island of Porto Santo. 9-12 July 2018. pp. 1-7.

67. Alfa Laval AB. Global provider in the areas of heat transfer, separation and fluid handling. https://www.alfalaval.nl/. (2021).

68. Crowley, M.F.o.S., GB) (2020) Near isothermal machine. United States patent application 10655618.

69. Knox, J. (1914). The Fixation of Atmospheric Nitrogen (Gurney & Jackson).

70. Aqua Forte Aeration. Membrane air compressor v-30m. https://www.aqua-forte.com/productgroups/aeration/. (2021).

71. Amano, H., Baines, Y., Beam, E., Borga, M., Bouchet, T., Chalker, P.R., Charles, M., Chen, K.J., Chowdhury, N., Chu, R., et al. (2018). The 2018 GaN power electronics roadmap. Journal of Physics D: Applied Physics *51*, 163001. 10.1088/1361-6463/aaaf9d.

72. Rusanov, V.D., and Fridman, A.A. (2007). The physics of a chemically active plasma (Taylor and Francis, CRC 1st edition).

73. Mutel, B., Dessaux, O., and Goudmand, P. (1984). Energy cost improvement of the nitrogen oxides synthesis in a low pressure plasma. Rev. Phys. Appl. (Paris) *19*, 461-464.

74. Pei, X., Gidon, D., and Graves, D.B. (2019). Specific energy cost for nitrogen fixation as NO x using DC glow discharge in air. Journal of Physics D: Applied Physics *53*, 044002. 10.1088/1361-6463/ab5095.

75. Patil, B.S., Cherkasov, N., Lang, J., Ibhadon, A.O., Hessel, V., and Wang, Q. (2016). Low temperature plasma-catalytic NOx synthesis in a packed DBD reactor: Effect of support materials and supported active metal oxides. Applied Catalysis B: Environmental *194*, 123-133. https://doi.org/10.1016/j.apcatb.2016.04.055.

76. Pei, X., Gidon, D., Yang, Y.-J., Xiong, Z., and Graves, D.B. (2019). Reducing energy cost of NOx production in air plasmas. Chemical Engineering Journal *362*, 217-228. https://doi.org/10.1016/j.cej.2019.01.011.

77. Moon, S.Y., and Choe, W. (2003). A comparative study of rotational temperatures using diatomic OH, O2 and N2+ molecular spectra emitted from atmospheric plasmas. Spectrochimica Acta Part B: Atomic Spectroscopy *58*, 249-257. https://doi.org/10.1016/S0584-8547(02)00259-8.

78.   Bruggeman, P.J., Sadeghi, N., Schram, D.C., and Linss, V. (2014). Gas temperature determination from rotational lines in non-equilibrium plasmas: a review. Plasma Sources Science and Technology *23*, 023001. 10.1088/0963-0252/23/2/023001.

79.   Vermeiren, V., and Bogaerts, A. (2020). Plasma-Based CO2 Conversion: To Quench or Not to Quench? The Journal of Physical Chemistry C *124*, 18401-18415. 10.1021/acs.jpcc.0c04257.

80.   Turner, M.M. (2016). Uncertainty and sensitivity analysis in complex plasma chemistry models. Plasma Sources Science and Technology *25*, 015003. 10.1088/0963-0252/25/1/015003.

81.   Treanor, C.E., Rich, J.W., and Rehm, R.G. (1968). Vibrational Relaxation of Anharmonic Oscillators with Exchange-Dominated Collisions. The Journal of Chemical Physics *48*, 1798-1807. 10.1063/1.1668914.

82.   Bogaerts, A., and Centi, G. (2020). Plasma Technology for CO2 Conversion: A Personal Perspective on Prospects and Gaps. Frontiers in Energy Research *8*. 10.3389/fenrg.2020.00111.

83.   S-Team Lab, B., Sklovakia (2021). HOMER-series STHT 2.45 GHz Autotuner with intergrated automatic impedance and power measurement system combined with a motorized 3 stub tuner. https://www.s-team.sk/products/autotuners.

84.   Bilik, V. (2002). Six-Port Measurement technique: principles, impact, applications. https://s-team.sk/docs/SixPortTechnique.pdf. Invited paper at the Radioelektronika-2002 Conference, Bratislava, Slovakia, 14-16 May 2002. S-TEAM lab.

85.   Emerson Rosemount™ X-STREAM X2GP Continuous Gas Analyzer. https://www.emerson.com/en-us/catalog/rosemount-x-stream-x2gp-continuous-gas-analyzer. (2020).

86.   Pancheshnyi, S., Eismann, B., Hagelaar, G.J.M., and Pitchford, L.C. (2008). Computer code ZDPlasKin. University of Toulouse, LAPLACE, CNRS-UPS-INP, Toulouse, France. www.zdplaskin.laplace.univ-tlse.fr

87.   Thompson, G.D.B.a.S. (2013). DVODE solver - ordinary differential equation (ode) solver - a Fortran 90 version of the well-known VODE ode solver by Brown, Byrne, and Hindmarsh.

88.   Hagelaar, G.J.M., and Pitchford, L.C. (2005). Solving the Boltzmann equation to obtain electron transport coefficients and rate coefficients for fluid models. Plasma Sources Science and Technology *14*, 722-733. 10.1088/0963-0252/14/4/011.

89.   Pintassilgo, C.D., Guerra, V., Guaitella, O., and Rousseau, A. (2014). Study of gas heating mechanisms in millisecond pulsed discharges and afterglows in air at low pressures. Plasma Sources Science and Technology *23*, 025006. 10.1088/0963-0252/23/2/025006.

90.   Capitelli, M., Ferreira, C.M., Gordiets, B.F., and Osipov, A.I. (2013). Plasma Kinetics in Atmospheric Gases (Springer Berlin Heidelberg).

91.   Saxena, S.C., and Chen, S.H.P. (1975). Thermal conductivity of nitrogen in the temperature range 350–2500 K. Molecular Physics *29*, 1507-1519. 10.1080/00268977500101321.

92.   Heijkers, S., Snoeckx, R., Kozák, T., Silva, T., Godfroid, T., Britun, N., Snyders, R., and Bogaerts, A. (2015). CO2 Conversion in a Microwave Plasma Reactor in the Presence of N2: Elucidating the Role of Vibrational Levels. The Journal of Physical Chemistry C *119*, 12815-12828. 10.1021/acs.jpcc.5b01466.
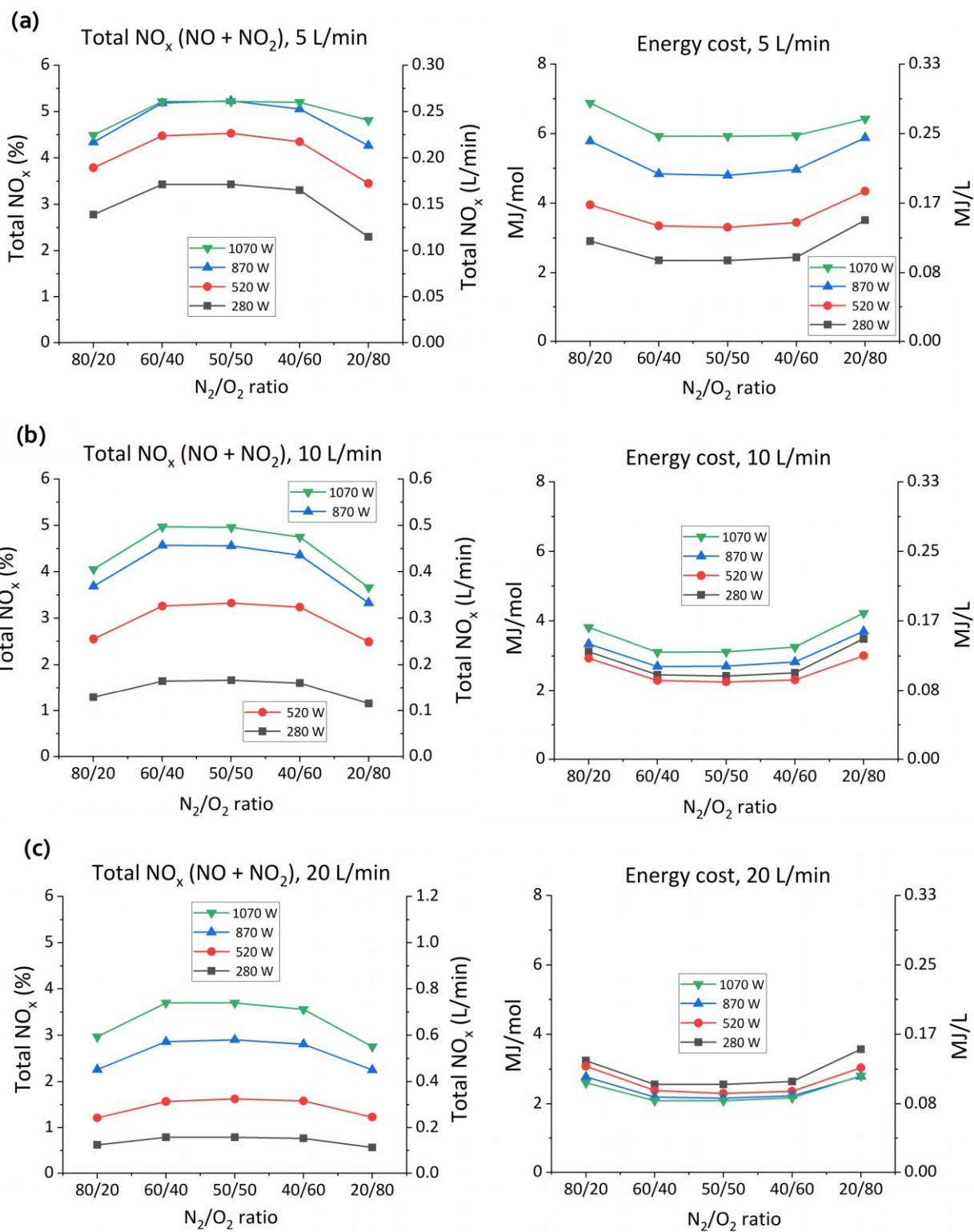
Figure 1: Experimental results for MW plasma in air and N_2/O_2 mixtures at atmospheric pressure: total NO_x concentration (% and L/min on right hand axis) and associated energy cost (MJ/mol and MJ/L) for a range of absorbed MW powers and mixture ratios, at flow rates of **a)** 5 L/min, **b)** 10 L/min, and **c)** 20 L/min. All measurements were performed in triplicate, but the errors bars are too small to be visible. The measured data for this figure is provided in the supporting information **SI, section S.3.3, table SI.2**.
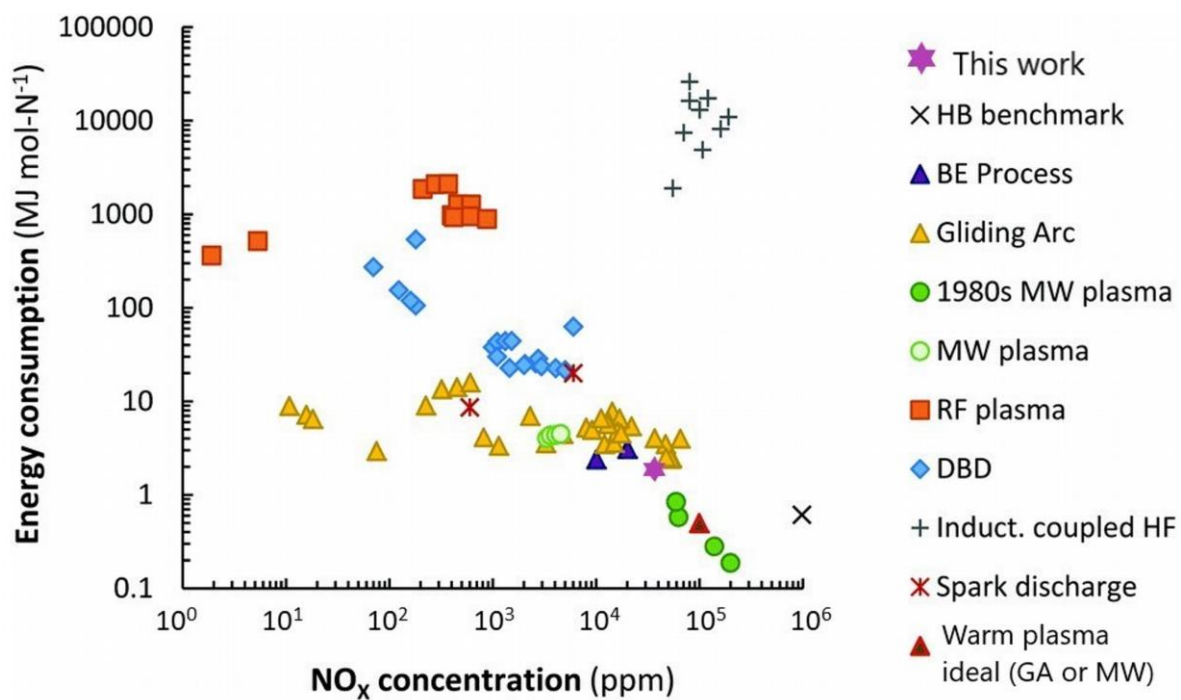
Figure 2: State-of-the-art for plasma-based NO_x formation (and HB benchmark), plotting energy consumption vs NO_x concentration. This figure is reproduced from Rouwenhorst et al.[7] to which our best results (i.e., ~3.8 % NOx at ~2 MJ/mol; see star legend) are added.
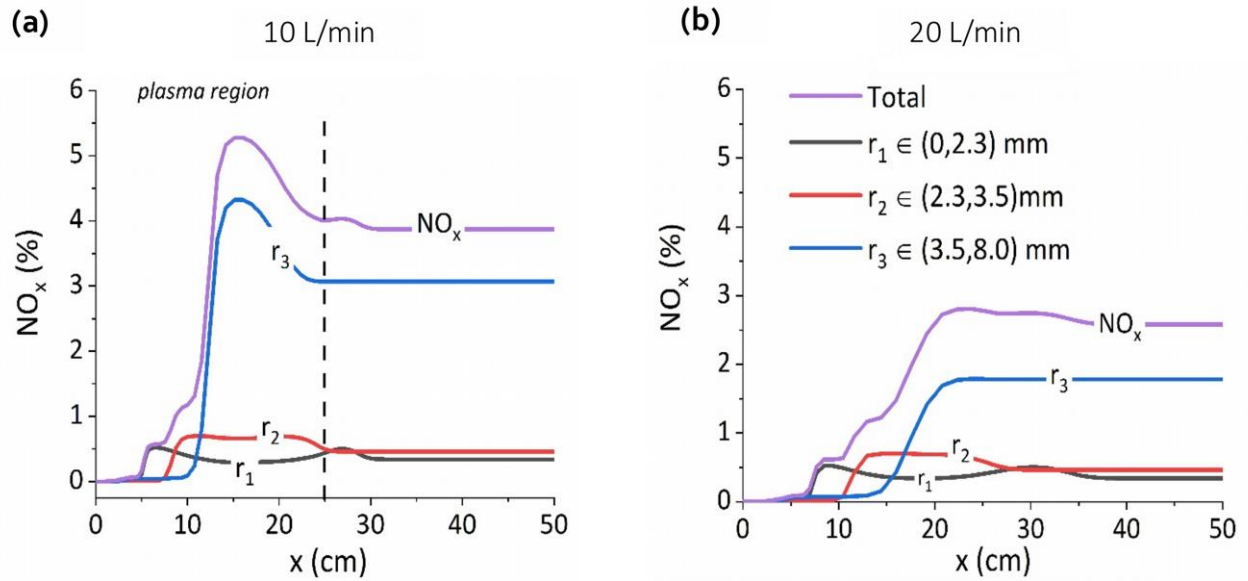
Figure 3: Quasi-1D modelling results of total NO_x concentration [%] at 870 W and N_2/O_2 ratio of 80/20 (dry air), for **a)** 10 L/min and **b)** 20 L/min mass flow rate, along the lateral (x) and radial (r) extent of the gas inside the quartz tube (inner radius 8 mm). The total NO_x concentration is the summation of the contributions from each radial section (i.e., r_1, r_2 and r_3); see **SI** for modelling details. The vertical dashed line at x = 25 cm indicates the end of the plasma.
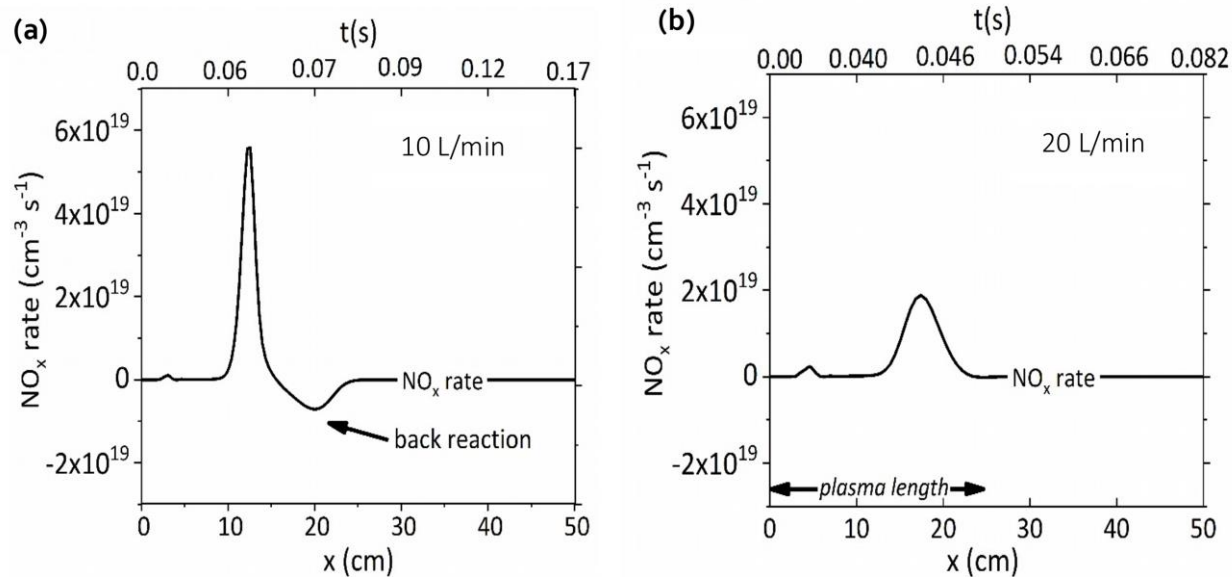
Figure 4: Quasi-1D modelling results of the total NO_x production rate [cm^{-3} s^{-1}] at 870 W, for **(a)** 10 and **(b)** 20 L/min, in the interval **3.5 < r_3 < 8 mm**. The negative rate results in NO_x loss due to back reactions (i.e., reverse **reaction 1**). The equivalent residence time t[s] is shown on the top x-axis: note the time tick marks correlate to the position axis at the specified times only and the spacing on the time axis is non-uniform due to the non-linear relationship between the position and residence time, given the dynamic gas velocity (see **section S.2.1** in **SI**).
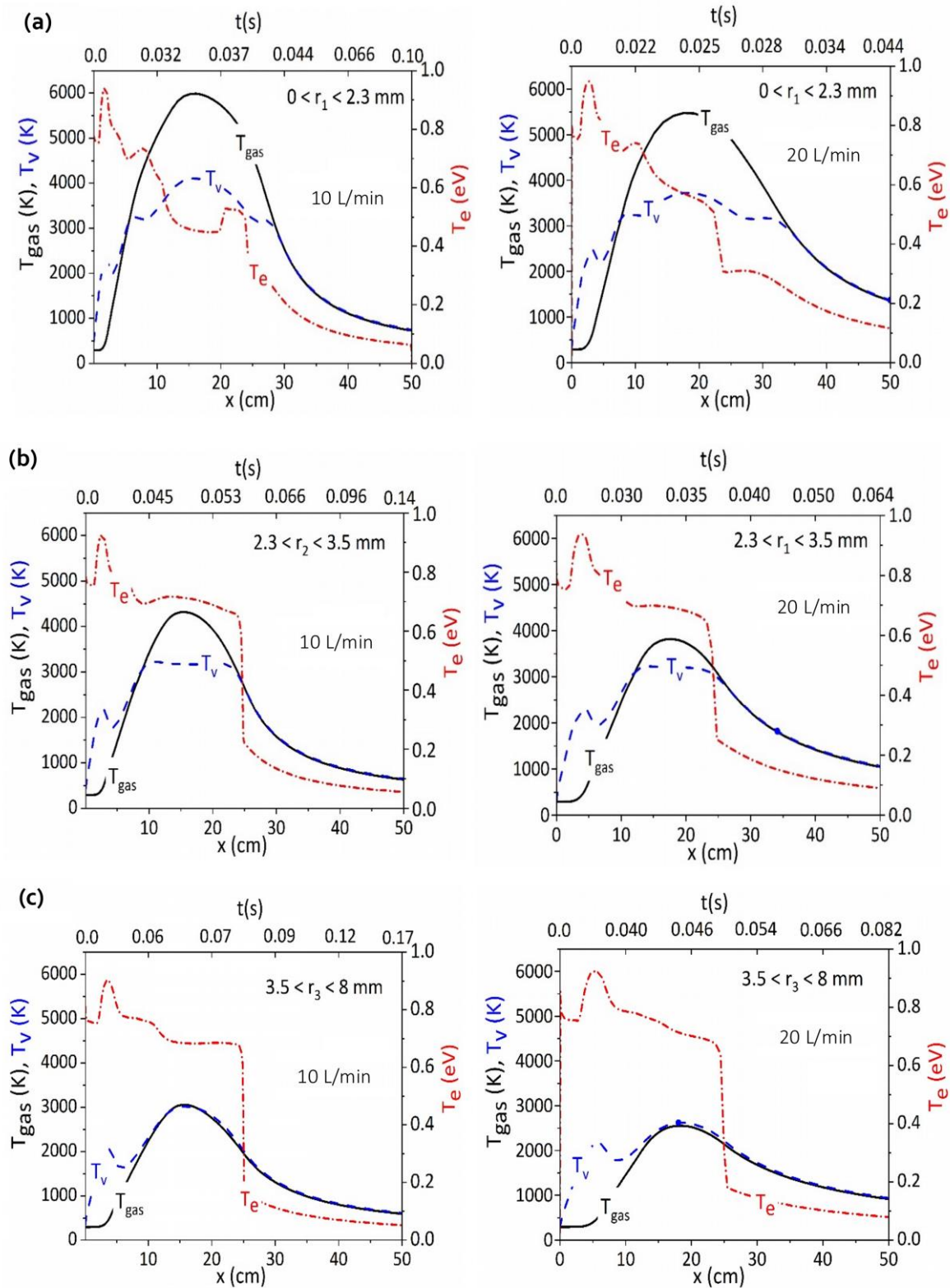
Figure 5: Quasi-1D modelling results of gas temperature (T_{gas} [K]), vibrational temperature of the first N_2 level with respect to ground state (T_v [K]) (left y-axis) and electron temperature (T_e [eV]) (right y-axis) at 870 W power for flow of 10 L/min (left) and 20 L/min (right), for three different radial regions: **(a)** $0 < r_1 < 2.3$ mm, **(b)** $2.3 < r_2 < 3.5$ mm, and **(c)** $3.5 < r_3 < 8$ mm. The equivalent residence time t[s] is shown on the top x-axis; note the time tick marks correlate to the position axis at the specified times only, and the spacing on the time axis is non-uniform due to the non-linear relationship between the position and residence time, given the dynamic gas velocity (see **section S.2.1** in **SI**).
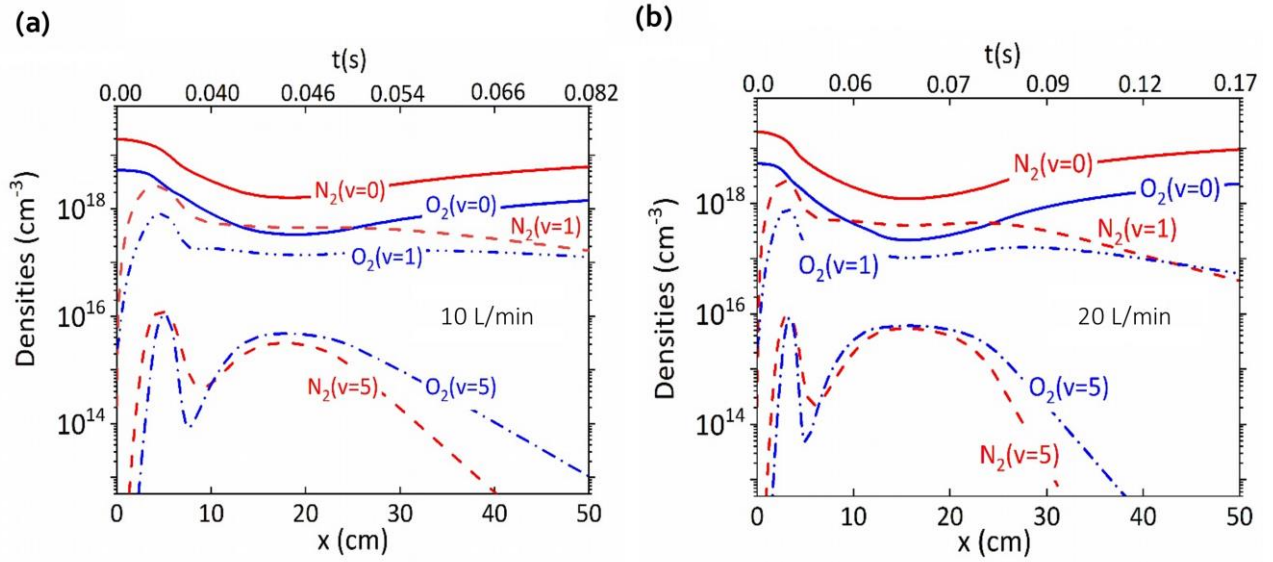
Figure 6: Quasi-1D modelling results of $N_2(v)$ and $O_2(v)$ level populations (for v=0, 1 and 5, where v=0 stands for the ground state) [cm^{-3}] at 870 W power, and **3.5 < r$_3$ < 8 mm**, for (**a**) 10 L/min and (**b**) 20 L/min. The equivalent residence time t[s] is shown on the top x-axis; note the time tick marks correlate to the position axis at the specified times only, and the spacing on the time axis is non-uniform due to the non-linear relationship between the position and residence time, given the dynamic gas velocity (see **section S.2.1** in **SI**).
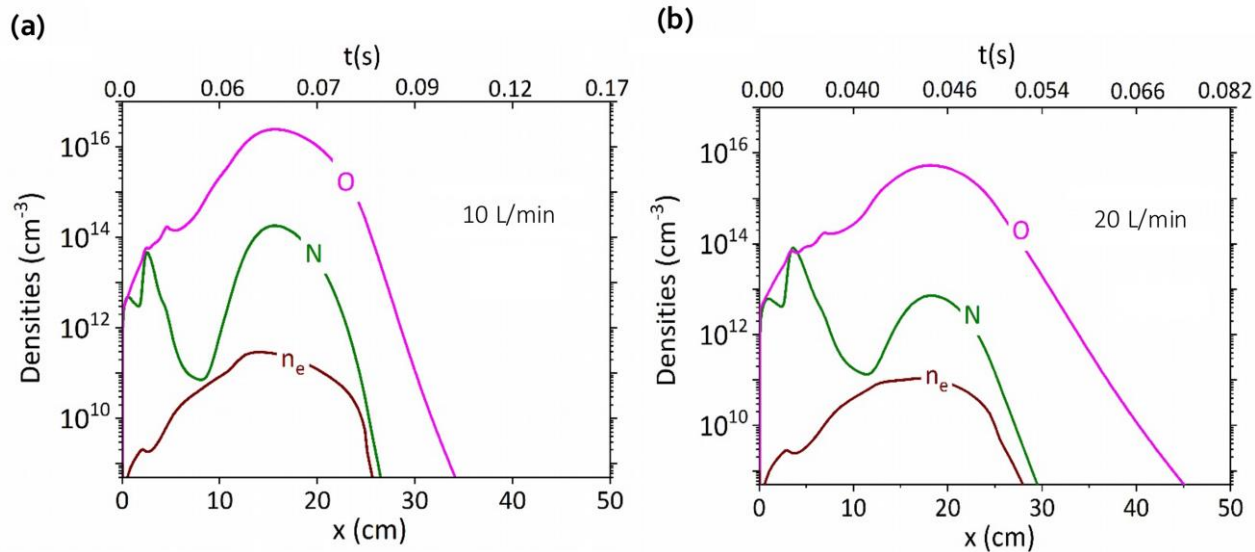
Figure 7: Quasi-1D modelling results of O, N and electron density [cm^{-3}] at 870 W power, **3.5 < r < 8 mm**, for **a)** 10 L/min and **b)** 20 L/min. The equivalent residence time t[s] is shown on the top x-axis: note the time tick marks correlate to the position axis at the specified times only, and the spacing on the time axis is non-uniform due to the non-linear relationship between the position and residence time, given the dynamic gas velocity (see **section S.2.1** in **SI**).
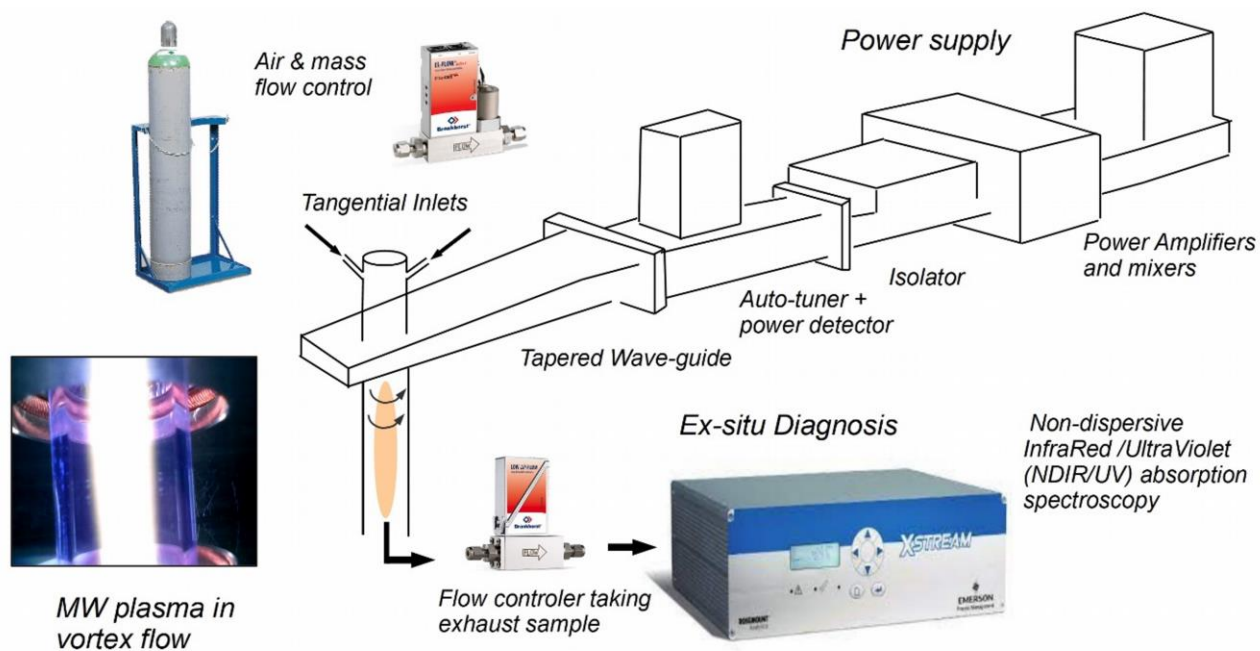
Figure 8: Experimental setup of our solid-state MW plasma power supply and tapered waveguide section for plasma ignition, including the exhaust diagnostic arrangement – the inset camera image illustrates the radial extent of the plasma filament inside the waveguide.
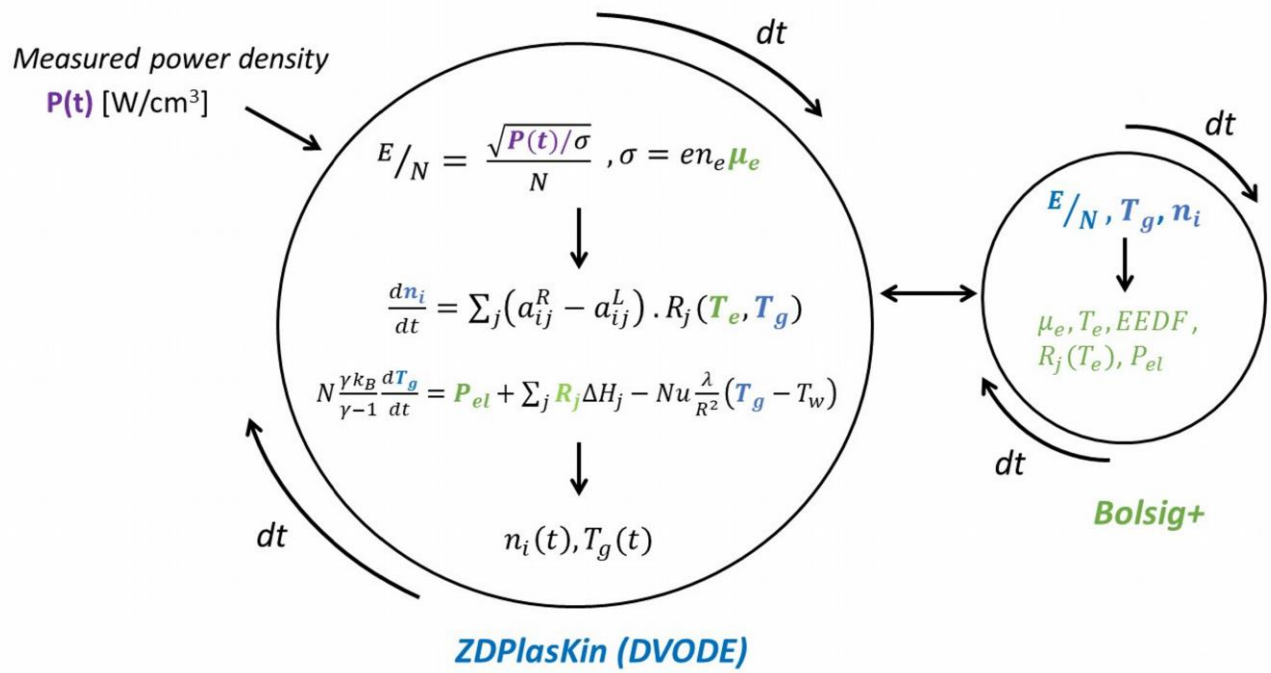
Figure 9: Overview of the numerical solution scheme for the quasi-1D model employing ZDPlasKin, which incorporates the DVODE code for ODE integration and BOLSIG+ to solve the Boltzmann equation at each time step. An experimentally determined power density [W/cm³] is coupled externally to enable solution via the reduced electric field E/N.

Table 1: State-of-the-art for plasma-based NO_x formation, in various plasma types, reporting the obtained NO_x concentration and energy cost, as well as flow rate and pressure used. Our best results are listed in the first row along with other notable MW reports. Non-MW reports are detailed in the bottom rows. This table serves as an abridged list of reactors given in **figure 2** above (see Rouwenhorst et al.[7] for further details) with equivalent NO_x % given here (i.e., 10,000 ppm = 1%).

Plasma type	NO_x %	Energy Cost	Flow rate [L/min]	Pressure [atm]	Ref.
Electrode-free MW plasma – swirling flow & surface wave mode	3.8 %	2 MJ mol^{-1} NO_x	20	~1	This work
Microwave (MW) plasma – electron cyclotron resonance	14%	0.28 MJ mol^{-1}	-	0.01	15,16,72
MW plasma with catalyst	6%	0.84 MJ mol^{-1} NO	0.33	0.07	73
MW plasma with pin – low power	0.6%	3.76 MJ mol^{-1} NO_x	6	~ 1	22
Birkeland-Eyde process: plasma arc with magnetic field	2%	2.0 – 3.28 MJ mol^{-1} HNO_3		~1	8,10
Gliding Arc Plasmatron (GAP)	1.5%	3.6 MJ mol^{-1} NO_x	10	~1	23
Rotating Gliding Arc (RGA)	5.5 %	2.5 MJ mol^{-1} NO_x	2	~1	24
Pin-to-pin DC glow discharge	0.7%	2.8 MJ mol^{-1} NO_x	10	~1	74
Packed DBD with catalyst	0.5%	18 MJ mol^{-1} NO_x	1	~1	75
DBD, spark, glow, Propeller Arc	0.6%	56 – 140 MJ mol^{-1} NO_x	1	~1	76